# SYNTHESIS OF MIXED METAL OXIDE BASED THIN FILMS A SUITABLE ALTERNATIVE FOR ELECTRO-OXIDATION OF METHANOL IN DIRECT METHANOL FUEL CELL


**Karishma Mahmood**

**Reg.No: 00000278303**


**This work is submitted as a MS thesis in partial fulfillment of the requirement for the degree of**

**(MS in Chemistry)**

**Supervisor's Name**

**Dr. Muhammad Adil Mansoor**


**Department of Chemistry**

**School of Natural Sciences (SNS) National University of Sciences and Technology (NUST), H-12**

**Islamabad, Pakistan**

FORM TH-4

# National University of Sciences & Technology

## MS THESIS WORK

We hereby recommend that the dissertation prepared under our supervision by: KARISHMA MAHMOOD, Regn No. 00000278303 Titled: Synthesis of Mixed Metal Oxide Based Thin Films A Suitable Alternative For Electro-Oxidtion of Methanol In Direct Methanol Fuel Cell Be Accepted in partial fulfillment of the requirements for the award of **MS** degree.

**Examination Committee Members**

1. Name: PROF. MUHAMMAD MAZHAR Signature: 02-11-2021

2. Name: PROF. MANZAR SOHAIL Signature: 02/11/21

External Examiner: DR. ALI HAIDER Signature:

Supervisor's Name DR. M. ADIL MANSOOR Signature: 02/11/2021

Head of Department

2/11/21
Date

**COUNTERSINGED**

Date: 2/11/21

**Dean/Principal**

## ACKNOWLEDGEMENTS

I am grateful to Allah Almighty, who granted me power, life, peace and courage to conduct this research. I would like to deliver my sincere gratitude people who helped me with this project.

First and foremost, I would like to thank my supervisor, **Dr. Muhammad Adil Mansoor** for his support and guidance. It would have been next to impossible to finish this thesis writing without his continual guidance and commitment. I would like to forward a kind of acknowledgement to **Dr. Mudassir Iqbal** who helped me in accomplishing my research work by providing chemicals and helping me in characterization of sample. I would share my warm gratitude to all my **friends** who helped me throughout my research work and provide me valuable suggestions, and to the lab attendant for being so cooperative and humble during my research work.

I am greatly appreciative of academic staff of **SNS** for being so helpful and friendly in taking care of my academic welfare. Last but not the least I want to acknowledge myself for not giving up and for being consistent and patient about all the difficulties and hardships I have faced throughout the completion of my thesis.

**KARISHMA MAHMOOD**

## Abstract

The present work focused on the fabrication of cost friendly electro-catalysts for the oxidation of methanol with enhanced efficiency. NiO, $ZrO_2$, $Y_2O_3$, NiO-$ZrO_2$/FTO and NiO-$Y_2O_3$/FTO thin films were deposited on FTO glass substrate via simple deposition method. Different characterization techniques were used to characterize the prepared thin films. SEM confirmed the uniformity and porosity while EDS confirmed the elemental composition of the prepared thin films. Other techniques like XRD, Raman spectroscopy and FTIR revealed the crystallinity phases and successful formation of mixed metal oxide thin films without any additional impurities.

Electrocatalytic behaviour of prepared thin films towards methanol oxidation was studied using potentiostat based on three electrode system, in 0.5M NaOH electrolyte solution at scan rate of 100 mV/s, using Pt wire as counter electrode, Ag/AgCl as reference electrode and prepared metal oxide composite thin film as working electrode, providing potential range of -0.5 to 2.0V. Different electrochemical techniques like cyclic voltammetry (CV), electrochemical impedance spectroscopy (EIS), chronoamperometry (CA) studies were performed to evaluate the efficiency of prepared metal oxide thin films for methanol oxidation. NiO-$Y_2O_3$/FTO thin film showed current density value of 7 mA/cm$^2$ vs. 0.65 V with 0.8 M methanol solution at scan rate of 100mV/s. NiO-$ZrO_2$/FTO thin film showed current density value of 10 mA/cm$^2$ vs. 0.65 V with 0.6 M methanol solution at scan rate of 100mV/s. Comparatively, pure NiO,$Y_2O_3$ and $ZrO_2$observed no prominent oxidation peaks which is attributed to the synergistic effect between metal oxides in mixed metal oxide thin films (NiO-$Y_2O_3$/FTO and NiO-$ZrO_2$/FTO) .

Furthermore, it was found that with increase in methanol concentration and scan rate, current densities of the prepared thin films increases, which inferred that oxidation of methanol is diffusion-controlled process and increase in scan rate increases electron transfer process which ultimately enhances the peak current density. Concentration studies revealed that thin films with 0.1: 0.1 (NiO: $Y_2O_3$/$ZrO_2$) precursor concentration showed best results with oxidation peak at the lowest oxidation potential and lowest onset potential. Current-time plot was obtained to check the stability of prepared thin films towards methanol oxidation. NiO-$ZrO_2$/FTO and NiO-$Y_2O_3$/FTO thin films observed current decay of 10% and 6.8% of initial current density values. This decay may be due to the reduction of methanol concentration near electrode surface with time or due to accumulation of carbonaceous reaction

intermediates like CO on electrode surface. Electrochemical impedance studies were conducted to further evaluate the electrocatalytic performance of prepared films. Nyquist plot of NiO-$ZrO_2$/FTO showed decreased $R_{ct}$ value of 34.14Ω compared to pure NiO and $ZrO_2$ with $R_{ct}$ values of 88.42Ω and 2779Ω, respectively. Nyquist plot of NiO-$Y_2O_3$/FTO showed decreased $R_{ct}$ value of 22.8Ω compared to pure NiO and $Y_2O_3$ with $R_{ct}$ values of 88.4Ω and 3189Ω, respectively. These mixed metal oxide thin films showed enhanced catalytic performance, high stability and reusability which make them the best alternatives for methanol oxidation reactions.

# TABLE OF CONTENTS

# LIST OF FIGURES

# List of Tables

# CHAPTER 01

## Introduction

The unexpected tremendous increase in population and industrialization has dramatically increased the demand of energy. According to published report by International Energy Agency (IEA) energy demand will increase by 30% till 2040 globally [1]. Another report by US Energy Information Administration (EIA) revealed that the use of energy in both Economic Cooperation and Development (OECD) and non-OECD countries was same by the year 2007. While non-OECD countries are expected to enhance their energy demand by 84% and OECD countries by 14% till 2035, respectively [2]. Moreover, the rapid increase in the use of technology is highly dependent on energy utilization in the form electricity. All the electronic devices need power source to be operated. Pakistan relies on hydro power plants and fossil fuels for generation of electricity which is still not sufficient to fulfil the increasing demand of electricity throughout the country. Hence generation of energy using feasible and efficient techniques is the current global concern.

Furthermore, fossil fuels are used as top sources for electric power generation which adversely affect the environment. Currently, the largest sources of fossil fuel energy are crude oil (39%), followed by coal (33%) and natural gas (28%) [3]. It is reported that approximately 40% of coal, 4% oil and 22% gas is used for electricity production on global level which contributes to increasing level of $CO_2$ in the atmosphere [4]. Although, fossil fuels are not likely to grow swiftly as compared to non-fossil fuels such as nuclear power and the renewable energy, yet it is estimated that for next 20 years that about 80% of energy will be consumed through burning of fossil fuels. Thus, this unavoidable dependence on fossil fuels for energy use is inescapable [5]. Plenty of research work has been done to find renewable, efficient and eco-friendly alternative strategies for power generation.

From the last decade fuel cells are popular as best alternative to meet the demands of energy generation due to their improved efficiency, cost-friendly and environment-friendly characteristics compared to other power generating devices. Fuel cells are power generating devices that undergo conversion of electrochemical reactions of fuels into electrical energy with the production of non-toxic by-products. The general assembly of a fuel cell constitute a cathode, an anode and an electrolyte membrane which separates them. The $H^+$ ions from decomposition of hydrogen at anode move towards cathode by passing through an electrolyte membrane. An external circuit helps to transfer the electrons generated at the anode towards

cathode in order to stabilize the system. At cathode the electrons and hydrogen ions combine with oxidant ($O_2$) to produce water [6]. Figure 1 shows schematic representation of typical hydrogen oxygen fuel cell [7].

At anode: $H_2 \longrightarrow 2H^+ + 2e^-$

At cathode: $O_2 + 2H^+ + 2e \longrightarrow H_2O$

Overall reaction: $H_2 + O_2 \longrightarrow H_2O$

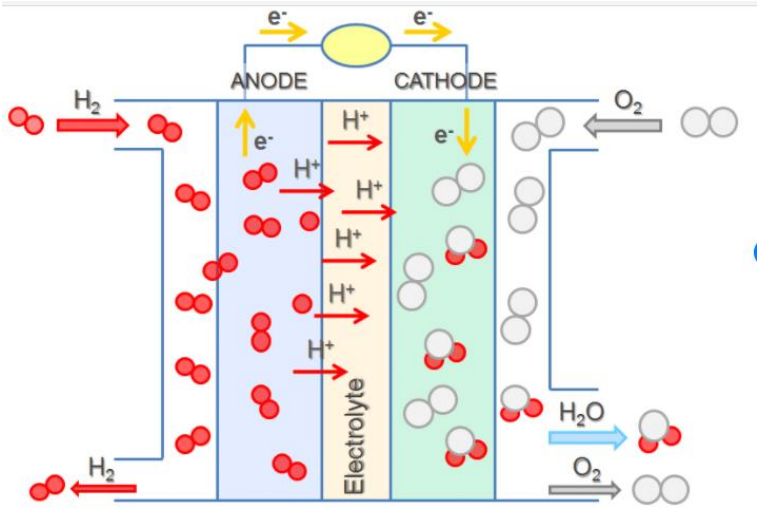


Fig; 1 Schematic representation of hydrogen-oxygen fuel cell.

### 1.1 Electrocatalysis and Methanol oxidation

Currently, direct alcohol fuel cells have got popularity as alternative sources for electric power generation. Direct methanol fuel cells use methanol as a fuel for electric power generation. Methanol is relatively preferred because of its easy availability usually derived from coal, oil or natural gas, easy handling, less toxicity, low cost and has low molecular weight and simple structure. The uprising direct methanol fuel cell (DMFC) technologies are associated with characteristics like low cost, eco-friendliness, portability, simple assembly and ease of operation, respectively. Furthermore, DMFC does not need an external power source to recharge rather it works on a refuelling system at low operational temperature. DMFCs with higher efficiencies and extended lifetimes can also be developed [8]. However, DMFCs still encounter challenge like high manufacturing costs which make their commercialization unfavourable. Other issues like methanol crossover from anode to cathode, lesser long-term stability, difficulty in managing water and heat and many other

complications have posted challenges to the operation of direct methanol fuel cells. However, many researchers have suggested plenty of advanced routes to overcome the barriers to the operation of methanol oxidation fuel cell and help in its commercialization [9].

### 1.2 Working principle of DMFC

Direct methanol fuel cells are advantageous to hydrogen fuel cell by the fact that there is no need of heavy reformer for production of $H_2$ gas from carbonaceous fuels and also it is easy to store and carry liquid methanol than hydrogen gas. Direct methanol fuel cells electrochemically oxidize methanol to carbon dioxide and water and covert its chemical energy to electrical energy. A typical DMFC constitute an anode (fuel electrode), cathode (oxidant electrode) and an electrolyte membrane separating both the electrodes. Figure 2 shows schematic representation of direct methanol alkaline fuel cell [9]. At the anode methanol oxidizes to produce water, carbon dioxide and six electrons. These electrons freely migrate to the cathode through external loaded circuit. At cathode the fed oxygen is electro-catalytically reduced to $OH^-$ ions by migrated electrons, the hydroxyl ions then migrate towards anode and oxidize methanol. The potential difference created at both the electrodes due to difference in number of electrons at anode and cathode facilitate the movement of electrons from anode to cathode and driving an electric current in the external loaded circuit. Theoretical calculations presented in literature suggest attainable Voltage of an approximate value 1.21V (against SHE) from methanol oxidation, but this value is not achievable in real practice due to several challenges associated with DMFC operation. The electrode reactions with standard potential (against SHE) are given as follows [10]

At anode: (methanol oxidation)

$$CH_3OH + 6OH^- \longrightarrow CO_2 + 5H_2O + 6e^- + Heat \qquad E^\circ = -0.81\ V$$

At cathode: (oxygen reduction)

$$3/2O_2 + 3H_2O + 6e^- \longrightarrow 6OH^- + Heat \qquad E^\circ = 0.40\ V$$

Overall reaction:

$$CH_3OH + 3/2O_2 \longrightarrow CO_2 + 2H_2O + Heat \qquad E^\circ = 1.21\ V$$

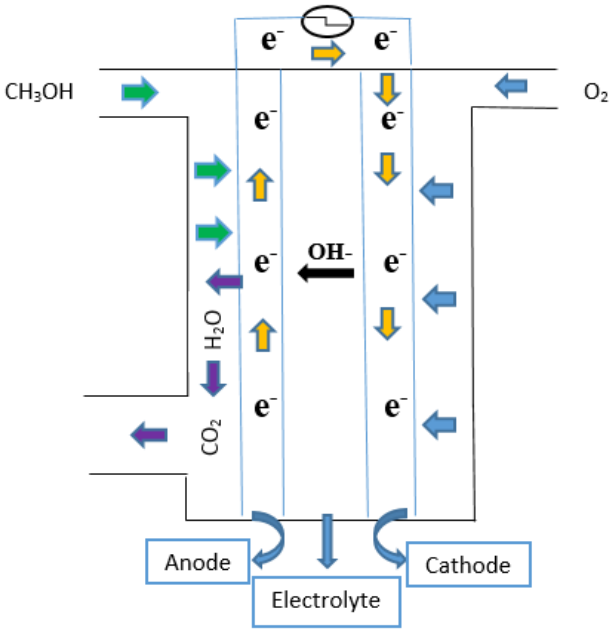


Fig; 2 Schematic representation of direct methanol alkaline fuel cell.

### 1.3 Mechanism of methanol oxidation

Mechanism of methanol oxidation is complicated. The process proceed through complex reactions of carbonaceous intermediates formation via different pathways to production of final oxidation products $CO_2$ and water. The basic steps include adsorption of $OH^-$ ions and methanolic intermediates on metal surface through electron transfer and hydrogen abstraction reactions followed by oxidation of the adsorbed intermediates by the adsorbed OH to $CO_2$ [11]. Figure 3 displays schematic representation of methanol oxidation mechanism.

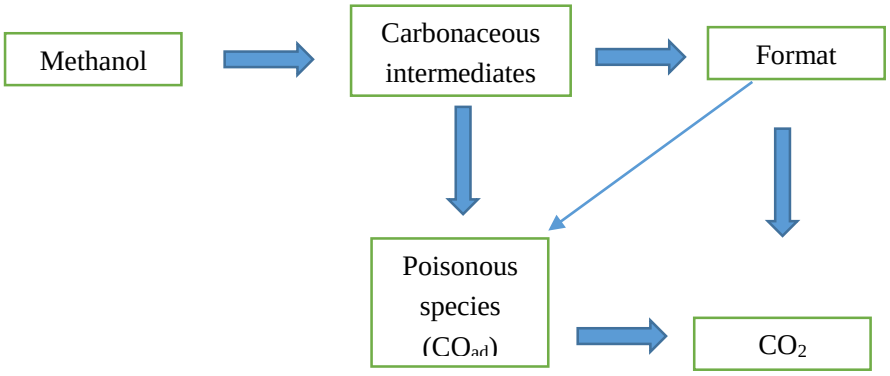


**Fig; 3 schematic representation of methanol oxidation mechanism**.

It is reported that the formation of $CO_{ad}$ species cause poisoning of electrode and decrease in methanol oxidation peak current, also $CO_2$ and format are the main soluble oxidation products in alkaline medium [12]. First, adsorption of hydroxide ions on catalyst surface leads to formation of metal hydroxide. The hydrous oxide formed actually provides oxygen sites for electrocatalytic oxidation of methanol (equation 1 and 2) [13].

The reactions at electrode-electrolyte interface are as follows;

The reactions at electrode-electrolyte interface are as follows;

$$M + OH^- \rightarrow M\text{–}(OH)_{ads} + e^- \quad (1)$$

$$M + 6OH^- \rightarrow [M(OH)_6]^{2-} + 4e^- \quad (2)$$

Proposed mechanism for dissociative chemisorption of methanolic species on anodic surface proceeds through following steps: Mahapatra, 2011 #398}

$$M + (CH_3OH)_{sol} \rightarrow M\text{–}(CH_3OH)_{ads} \quad (3)$$

$$M\text{–}(CH_3OH)_{ads} + OH^- \rightarrow M\text{–}(CH_3O)_{ads} + H_2O + e^- \quad (4)$$

$$M\text{–}(CH_3O)_{ads} + OH^- \rightarrow M\text{–}(CH_2O)_{ads} + H_2O + e^- \quad (5)$$

$$M\text{–}(CH_2O)_{ads} + OH^- \rightarrow M\text{–}(CHO)_{ads} + H_2O + e^- \quad (6)$$

$$M\text{–}(CHO)_{ads} + OH^- \rightarrow M\text{–}(CO)_{ads} + H_2O + e^- \quad (7)$$

$$M\text{-}(CHO)_{ads} + Pt\text{-}(OH)_{ads} + OH^- \rightarrow M + M\text{-}(COOH)_{ads} + H_2O + e^- \quad (8)$$

$$M\text{–}(CO)_{ads} + OH^- \rightarrow M\text{–}(COOH)_{ads} + e^- \quad (9)$$

$$M\text{–}(COOH)_{ads} + M\text{-}(OH)_{ads} \rightarrow M + CO_2 + H_2O + e^- \quad (10)$$

$$M\text{-}(COOH)ads + OH^- \rightarrow M\text{-}(OH)_{ads} + HCOO^- \quad (11)$$

$M\text{–}(CHO)_{ads}$ and $M\text{–}(CO)_{ads}$ can also be directly converted to $CO_2$ and water in the presence of suitable alkaline solution by following steps.

$$M\text{–}(CHO)_{ads} + Pt\text{-}(OH)_{ads} + 2OH^- \rightarrow M + CO_2 + 2H_2O + 2e^- \quad (12)$$

$$M\text{–}(CO)_{ads} + M\text{-}(OH)_{ads} \rightarrow M + CO_2 + H_2O + 2e^-. \quad (13)$$

The rate determining step is the oxidation of carbonaceous intermediate –CHO. In alkaline medium the boding of –CHO specie with catalyst electrode is not that strong, that is why its

further oxidation takes place without much difficulty. –CO species bonded strongly to the electrode surface which makes their complete removal impossible at low potential. While at higher potential availability of active oxygen species facilitates the complete removal of adsorbed -CO species.

The most accepted mechanism for reduction of oxygen at cathode is presented by Damjanovic et al [10]. They presented two possible pathways for ORR. One is direct reduction of oxygen to water through transfer of 4-electrons. Another shows formation of hydrogen peroxide intermediate through 2-electron transfer process as shown in following reactions.

**Path 1;**

$$O_2 + 2H_2O + 4e^- \rightarrow 4OH^- \qquad (14)$$

**Path 2;**

$$O_2 + e^- \leftrightarrow O_2^- \qquad (15)$$

$$O_2^- + H_2O \rightarrow HO_2^- + OH \qquad (16)$$

$$OH + e^- \leftrightarrow OH^- \qquad (17)$$

The drawback of using alkaline solution is carbonates formation as a result of reaction of produced $CO_2$ with OH ions. This results in decrease of electrolyte concentration and blocking of active sites for methanol adsorption and oxidation. Continuous removal of produced $CO_2$ gas, circulation of the electrolyte solution or use of electrolyte membranes can overcome these problems [12].

### 1.4 Factors effecting methanol oxidation reaction

#### 1.4.1 Morphology

Studies have reported that nanostructured anode materials with porous surface and controlled pore-size showed best electrocatalytic performance towards methanol oxidation which is attributed to enhanced mass and charge transfer and increased active sites. Reportedly, modulation of Pt electrode with such mesoporous materials not only enhanced the catalytic performance of electrode but also increased its durability and stability [14].

Tang et al. presented a study on effects of size and shape on electrocatalytic performance of the electrode material towards oxidation of methanol and reduction of oxygen. They fabricated ITO-deposited Au nano-materials of different dimensions (20nm nano-spheres,

45nm nano-spheres and 20 × 60 nm nano-rods) and investigated their catalytic performances. Nano-spheres of size 20nm showed current density of value 11.00 mA $mg^{-1}$ compared to 45nm nano-spheres with current density of value 5.59 mA $mg^{-1}$ which is associated with small size nano-spheres with large surface to volume ratio and enhanced charge transfer process and catalytic performance. Nano-rods showed peak current density of value 0.91 mA $mg^{-}$ compared to other nano-morpholigies. This result was attributed to the exposure of active (111) facets in nano-spheres. Generally it was concluded that methanol oxidation is morphology dependent process [15].

### 1.4.2 Acidity and basicity of electrolyte

Acid/basic electrolytes effect the oxidation of methanol. It is reported that most of the electrocatalysts function better in alkaline medium. Alkaline medium facilitates weak bonding of carbonaceous products to the electrode and hence enhanced catalytic performance while acidic media promote strong bonding of carbonaceous products to the electrode surface which shifts the oxidation peak potential to higher value and cause poisoning of the electrodes. Furthermore, the hydroxyl ions in alkaline electrolyte solution get adsorbed on catalytic surface and promote oxidation of methanol even at lower potential. It is also reported that the kinetics of cathode oxygen reduction reaction is well fitted in alkaline media [16]. Studies proposed that methanol cross-over issue is reduced in alkaline media compared to acidic media because the flow of anions is opposite in direction to that of proton flow which results in reversed electro-osmotic drag and reducing methanol crossover [10].

Tripković et al reported Pt/Ru electrocatalyst with different Ruthenium loadings and observed that platinum catalyst of 47.5 wt% showed peak current density of value 17.6 mA $mg^{-1}$ in 0.1M NaOH electrolyte solution at 295 K, whereas same catalyst gave current density of value 3.1 mA $mg^{-1}$ in 0.5M $H_2SO_4$ electrolyte solution at same temperature due to increased competition between $OH_{ads}$ and bisulphate anions for adsorption onto the electrode surface in acidic medium [16c]. As discussed above alkaline DMFCs undergo formation of carbonates which degrade the catalytic performance of electrodes. The hydroxide ions present at anode react with $CO_2$ and produce carbonate or bicarbonate. Hence at anode the ions neutralizing the charge present will be of $HCO_3^-$ and $CO_3^{2-}$. Whereas cathode continuously produce hydroxyl ions which give rise to a difference of pH at both electrodes and ultimate reduction of current density [17].

### 1.4.3 Catalyst support

One of the main parameter which influence the catalytic behaviour of catalyst material is the type of support used. Different studies conducted using different support materials revealed that type of supports influence properties like morphology, stability, porosity, surface area, CO-tolerance and current density of the catalyst electrode. Many support materials with characteristics like highly corrosion resistant, large surface area, high porosity and good interaction with electrode are reported as best support materials for electrocatalysts [9]. Kim et al. studied the electrocatalytic performance of conductive polymer (Polyaniline) supported PtRu catalysts and it was observed that PtRu/ PAni showed better results than PtRu/ C electrode, which was attributed to reasons like high electrical conductivity, high ions diffusion rate and larger surface area of PAni support compare to that of Carbon [18].

One of the most widely used support material is carbon black, usually used for the support of platinum based catalysts due to its certain properties like high electrical conductivity, large surface area and stability at acidic/basic pH. Yabei et al. fabricated Sn-$TiO_2$-carbon black supported Pt electrocatalyst and studied its electrocatalytic performance with respect to Sn doping and ratio of Sn-$TiO_2$ to carbon black. $Ti_{0.9}Sn_{0.1}O_2$–C electrocatalyst showed enhanced current density compared to that of Pt/$TiO_2$–C and Pt/C catalysts. It was deduced that Pt nanoparticles of 2 to 3 nm in size were deposited on the edges of $Ti_{0.9}Sn_{0.1}O_2$–C which leads to the formation of triple junction that increases the overall electrochemical surface area of the nanoparticles. Additionally, the presence of high amount of OH groups on $Ti_{0.9}Sn_{0.1}O_2$–C surface made the catalyat-support interactions stronger [19].

Carbon nanofiber is another widely used class of carbon support for modulation of electrocatalysts. CNFs are cylindrical nanostructured layered graphene with high surface area. Xue et al. reported that Pt nanoparticles dispersed on Co-embedded coal based nanofiber showed excellent mass activity of value 78.5 $Ag^{-1}$ Pt, which was 50 times to that of Pt/Co-CF and Pt/coal-CF respectively. CNF provides large number of nucleation sites for deposition of well dispersed small-sized Pt nanoparticles, ultimately enhancing the catalytic efficiency [20]. As electrochemical processes are diffusion controlled hence use of mesoporous materials to attain appropriate pore size (2-50 nm) for diffusion of ions, is advantageous. Gui–fa and his team reported a study on the effect of shape of carbon support and elctrocatalyst loading on the electrocatalytic performance of the synthesized nitrogen-doped mesoporous carbon supported platinum, towards methanol oxidation. It was found that

catalyst prepared with 2D support exhibited well distributed smaller Pt nanoparticles as compare to the one synthesized with 2D support. Different characterization analysis revealed strong Pt-N bonds on the surface of catalyst resulted from strong interaction between the catalyst and support which enhanced the electrocatalytic activity ultimately [21].

Single-walled carbon nanotubes (exhibit large surface area) and multi-walled carbon nanotubes (exhibit good conductivity) are also been widely used as catalyst supports. Single hexagonal sheets of carbon are rolled up to form cylindrical carbon nanotubes. CNTs not only exhibit good electrical conductivity, large surface area and mechanical strength but also capable of structural modifications by adding other elements to their lattice. Another carbon based support graphene has also been used as catalyst support by various researchers due to its certain properties like high surface area, flexible morphology, high electric conductivity, porosity and stability [22].

The main drawback related with the use of carbon-based supports is their lower electrochemical stability, the carbon-support materials are observed to undergo structural collapse during operating conditions [23]. Different strategies like modulation of carbon support with other metals have been employed to overcome the stability and corrosion problem but still they set certain limitations to the performance of catalysts [24]. Thus the emphasis is on the fabrication of inexpensive, transparent, conductive, non-carbon, highly efficient and stable support materials as alternative to carbon-based materials. Recently, hetero-atom doped metal oxides like antimony doped tin oxide (ATO), fluorine doped tin oxide (FTO) and Indium tin oxide (ITO) have been popularly used as alternative supports for electrocatalysts in fuel cells. These support materials have shown enhanced stability compared to carbon-based supports, good interaction between the catalyst and support and improved electrical conductance. Stable metal oxide support framework hinders the agglomeration of electrocatalyst nanoparticles and stabilizes it [25]. It is reported that heteroatom anions (e.g $F^-$ in FTO) help in enhancing electrical conductivity, catalyst-support interaction and dissolution of Sn from $SnO_2$. Additionally, electrons transfer from FTO to catalyst occur due to the spillover effect which increases electron density on catalytic surface [26], [27]. A study revealed that strong interaction between the support and doped metal oxide supports results in decrease of adsorptive strength of the catalyst to oxygenated species ($O_{ad}$ and $OH_{ad}$) which leads to enhanced methanol oxidation at anode and oxygen reduction activity at cathode [27].

### 1.5 Catalysts for Direct Methanol fuel cells

Selection of the type of electro-catalyst greatly influences the performance of methanol fuel cells. Discovering new electrocatalysts with enhanced features, as alternative to typical noble metal catalysts is still a difficult challenge for the researchers in the field of electrochemistry. Recently, many electro-catalysts with characteristic features like high catalytic activity, CO-poisoning resistivity, less-cost, high stability and durability have been presented in the literature. Figure 4 displays the schematic representation of reported electrocatalysts for oxidation of methanol.

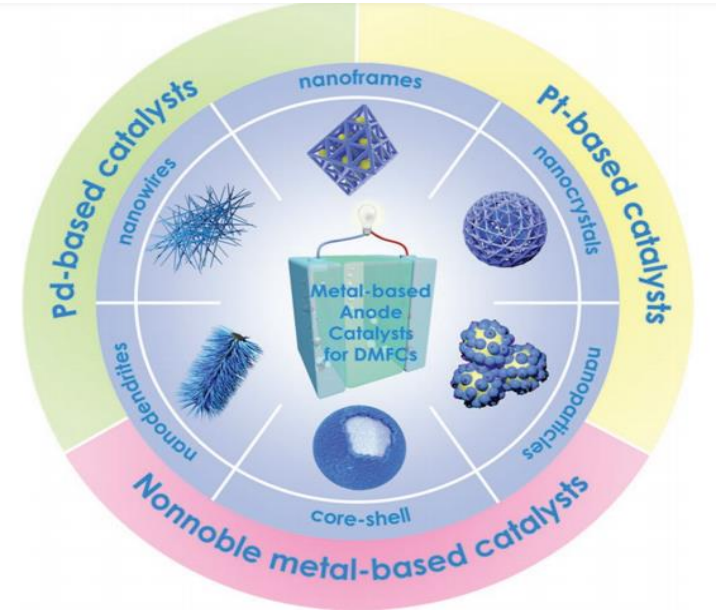


**Fig; 4 Schematic representation of reported electrocatalysts for oxidation of methanol**

#### 1.5.1 Electrocatalysts based on Noble metals

Noble metals such as Pd, Pt, Ru, Ag and Au have been widely used in fuel cell application. To enhance the catalytic efficiency of different noble metal based catalysts, electrocatalysts with different compositions and morphologies have been presented, varying from simple nanostructures like nanowires, nanotubes, nanofibers and nanospheres to complex morphologies like concave nanocubes, nanobowls, nanoframes, nanopolyhedras and core–shell electro-catalysts. Platinum based electro-catalysts are still a popular class of electroctalysts for DMFCs. Studies on Pt-based bimetallic and multi-metallic catalysts with improved properties have been reported. Liu et al. fabricated Ru@$Pt_{0.5}$/C electrode with Ru:Pt atomic ratio of 1:0.5. The prepared electrode showed enhanced catalytic performance towards methanol oxidation with mass activity of 1313.8 A/g and superior durability under

extreme electrochemical environment. Additionally, reduced CO poisoning was observed which was attributed to core-shell structure of the prepared catalyst [28].

Another study reported a series of Pd–Pt core–shell polyhedron catalysts of same sizes with different Pd:Pt ratios synthesized via seed-free and onze-pot method. Among the series of polyhedron catalyst, $Pd_{93}$–$Pt_7$ showed the best catalytic performance with the mass activity value of 165.9 mA/g. This exceptional behaviour of the prepared catalyst was attributed to the active sites exposure due to concave structure plus enhanced electron transfer process due synergistic effect between Pd and Pt [29]. Ling and team synthesized nanoporous Au bowls deposited Pt nanoparticles with improved catalytic performance and stability, via wet chemical fabrication technique. The catalyst was found resistant to Co-poisoning due to shifting of d-band to a new position resulted from synergistic effect between Pt and Au. This relocation of band weakened the adsorption of CO species to the catalytic surface and ultimately enhancing the overall catalytic performance [30].

Other than noble metals, less costly transition metals like Cu, Pb, Ni, Co and Sn with calculated sizes and regulated shapes have also been used in composites with Nobel metals for improved catalytic behaviour. Studies reported that addition of transition metals to heterostructures more likely results in locating the active sites on high index exposed facets on the surfaces of the catalysts. These facets usually exhibit loosely-coordinated atoms which contribute more actively to the MOR activity as compare to packed lower-index facets [31]. Furthermore, low cost and easy embodiment of transition metals into noble metals make their use even more advantageous. Shen and team fabricated hexagonal self-assembled array of PtCu nano-composite. The prepared catalyst showed enhanced electrocatalytic activity with peak current density of value 34.81 mA/cm and PtCu/C with peak current density of value 24.6 mA $cm^{-2}$, respectively. This enhancement was ascribed to the presence of highly active facets (111) planes on the catalytic surface. The reported electrocatalysts PtCu and PtCu/C also showed high durability and CO tolerance. A decay of only 12.28% was observed with PtCu nanocatalyst after 1000 scans of cyclic voltammetry, which was 3.9 times smaller than that observed with commercial Pt/C electrode [32].

Recently, Wen et al. synthesized tetra-hexahedral nono-frames of $Pt_3Ni$ alloy via carbon monoxide etching at high temperature. The nano-frames constitute high indexed facets of (510), (410), (310) and (720). It was reported that $Pt_3Ni$ nano-frames showed enhanced catalytic performance than $Pt_3Ni$ nano-crystals which was ascribed to down-shift of the d-

band center which results in shrinkage of outmost (200) lattice which indicated that the thin shell of Pt was was compressed to the core of Pt−Ni alloy. Additionally, the synergistic effect between Pt and Ni aroused due to contribution of d-electrons by Ni and adsorption of OH species on Ni surface for the removal of contaminating CO-species helped in enhancing the catalytic properties of the nano-frames even more [33].

The performance of Pt-catalysts towards methanol oxidation can be enhanced by modulating their composition and structures. Which result in in high porosity and stability, large surface area and increased active sites. Impregnation of other elements to Pt-based electrocatalysts introduce properties like synergistic effect, high-index facets, electronic effect and geometric effect, which help in enhancing the overall catalytic performance.

### 1.5.2 Electrocatalysts based on Non-noble metals

The major drawbacks associated with Pt-based catalysts, CO-poisoning, high cost and high activation over-potential make it necessary to investigate more catalysts with less cost, stable structure and efficient catalytic performance. Non-Noble metal based catalysts of low cost and high stability are considered to be promising alternates to noble metal based catalysts. Moreover, these non-noble metals are said to be very active and efficient in basic media compare to that of noble-metal catalysts. Until now, transition metals like Ni, Co, Cu, and their compounds have been widely used as elctro-catalysts due to their certain properties like cost-effectiveness, high abundance and excellent surface oxidation properties [34], [35]. But controlled-fabrication of the non-metal metal based catalysts is still a challenge.

Hu and team fabricated ITO deposited Ni–Ti nanoparticles film (Ni–Ti /ITO) via two step ion-implantation technique. The prepared Ni–Ti /ITO film observed higher catalytic oxidation compare to that observed with pure Ni/ITO and Ti/ITO, attributed to the closely packed and uniformly distributed nanoparticles in Ni–Ti /ITO which result in large surface area large number of active sites. Additionally, the adsorption of OH species to Ti surface improves CO-tolerance of the catalyst and improve the catalytic oxidation reaction kinetics [36].

Metal oxides are also been popularly used for efficient oxidation of methanol. It is reported that the oxygen element in metal oxides facilitates the efficient removal of the adsorbed carbonaceous intermediates (CO), thus greatly uplift the electro-catalytic performance. Peng and team fabricated Ni-foam deposited, nickel oxide nanosheet@nanowire array via hydrothermal technique. The prepared catalyst showed current density of value of 89 mA/cm

in 1M KOH electrolyte and 0.5 M methanol solution and loss of only 19% was observed after 1000 CV scans. This efficient performance of NiO NS@NW/NF catalyst was attributed to the good interaction between Ni foam and NiO nanosheets and 3D architectural design which facilitated charge transfer process and exposes large number of active sites for MOR. Additionally the binder-free synthesis made the catalyst performance free of interference resistance, active sites blockage and retardation of diffusion of ions [37].

Thamer et al. reported nitrogen doped carbon nanofibers incorporated Co synthesized via electrospinning technique. The electrocatalytic behaviour of the prepared catalysts with different nitrogen content (1-5% Urea) was investigated, the catalyst with 4% nitrogen content showed (Co/N(4%)-CNFs) showed maximum current density of value 100.84 mA/cm compared to other percentages of Nitrogen, ascribed to excellent adsorption capability and smaller charge transfer resistance values of the catalyst [38].

Mengqi et al. presented coral-shaped porous Ni-Co oxides ($NiCo_2O_4$) synthesized via additive free solvothermal decomposition strategy followed by calcination subsequently. According to Cyclic voltammetry results, coral-shaped $NiCo_2O_4$ exhibited higher current density (9.844 mA/cm) compare to that of moss-shaped $NiCo_2O_4$ catalyst (7.166 mA/cm). According to chronoamperometry results, coral-shaped $NiCo_2O_4$ showed less current decay with 72.53% retention of the original current density value, whereas, moss-shaped $NiCo_2O_4$ about 1.47% retention of current density which was attributed to the amorphous nature of moss-shaped $NiCo_2O_4$ [39].

Cu is much more resistant to CO-adsorbed species compare to other well-known metal electrocatalysts such as Pt, Ru, Pd and Rh, which ultimately help in promoting the catalytic performance. Ren et al synthesized Pd nanoparticles decorated ultra-long copper nanowires of 35 nm thickness via hydrometallurgy synthesis technique. Electrochemical analysis revealed that the prepared binary shell-core Pd-Cu nanowires exhibited enhanced catalytic activity and electrochemical stability [40].

Recently, Ali Doner et al. successfully synthesized alkaline leached CuZn/Cu electrocatalyst via electrodeposition technique. According to cyclic voltammetry results, CuZn/Cu exhibited peak current density of 297.14 mA/cm compare to that of Cu/Cu electrode which gave current density of 235.65 mA/cm. This enhancement was attributed to the large surface area, high porosity and synergistic electron transfer between Zn and Cu respectively [41].

## 1.6 Techniques for deposition of thin films

In the uprising world of Nanotechnology, reducing materials to nano sizes imparts unique properties to the materials. Performance of a material is greatly influenced by its surface properties. Different techniques are used for surface engineering to improve material's overall performance compared to bulk material, cost reduction and improving material's usage efficiency [42]. The thin film is defined as layer of material ranging from nanometres to few micro meters in thickness. Thin films are generated by deposition of atoms/molecules to the substrate, whereas thick film is generated by deposition of particles. Thin layer may constitute a homogeneous, microstructure single layer of the material or may consist of inhomogeneous multi layers of the material, depending upon the required properties for electrical, optical, optoelectronic or dielectric application. Thin films formation modifies chemical, magnetic, electrical, physical, electronic and mechanical properties of the bulk material [43]. All the techniques for thin films deposition follow four basic step [44], [45].

1) Preparation of the source for the material to be deposited.

2) Transportation of the source material to the substrate through a medium (fluid/vacuum depending on the type of technique)

3) Deposition of target material on the substrate, formation of thin film.

4) Calcination/annealing of the prepared thin film (if needed for the required properties of the film)

5) Characterization of thin film, results might help in modification of deposited thin film, if needed.

The atoms impinging from the source on the surface of substrate, lose energy and get deposited on the substrate through formation of bond with the surface atoms either via van der Waals interactions, metallic bonding or electrostatic interactions (ionic bond). These condensed atoms cluster together to form nuclei. The process of nucleation continues until a thin film of saturated density is obtained [45].

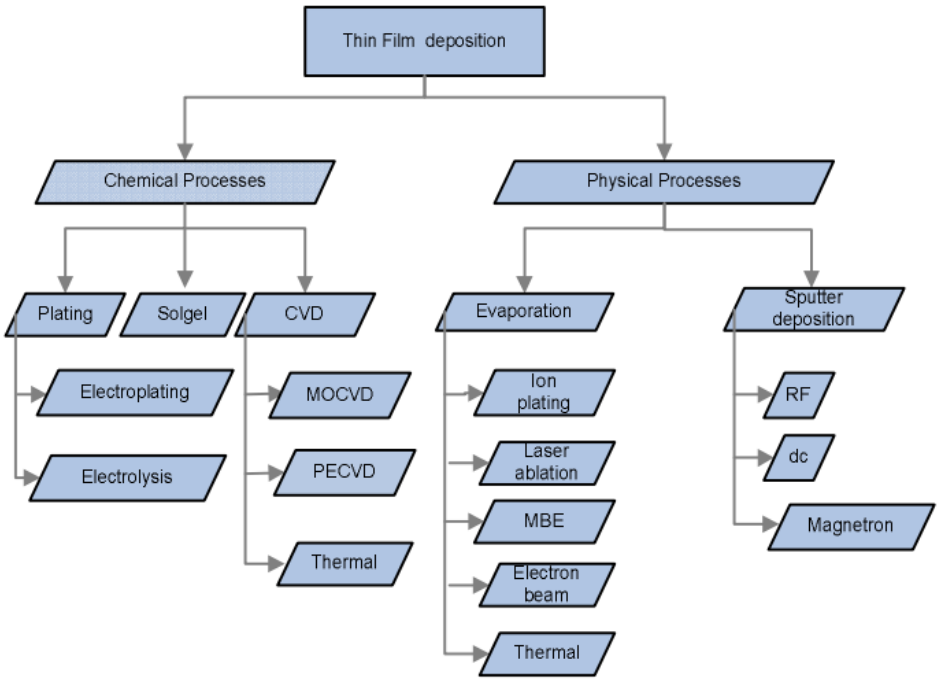


**Fig: 5 Schematic representation of different thin film deposition techniques**

### 1.6.1 Sol-gel technique

The sol–gel synthesis technique has been widely used for composition and structure-controlled deposition of highly pure, stable and homogeneous single or multilayers of metal oxide and ceramic powders on substrates. The process consists of formation of sol, a colloidal suspension of the precursor to be deposited, followed by conversion to viscous gel or solid film. Two routes are used for the preparation of precursor solution [46].

a) Preparation of the precursor solution by dissolving inorganic salts of metals in water.

b) Preparation of the precursor solution by dissolving metal-alkoxide in non-aqueous solvent.

The sol gel technique, involve polycondensation of metal alkoxide can be proceeded through following steps.

1) Dissolution of Chloride, nitrate or acetate salts of metals in alcohol.

(R= $CH_3$, $C_2H_5$….), (z= oxidation state of metal) [50].

$$(CH_3COO)_z\,M + zH\text{-}OR \Rightarrow M\,(OR)_z + zCH_3COOH$$

2) Hydrolysis, M-OR to M-OH

$$M\,(OR)_z + H_2O \Rightarrow M(OH)_z + zROH$$

3) Hydrolysis is followed by condensation (removal of water molecules) either by olation or oxolation process [47]. In olation process the metal centres are bridged through 'ol' (-OH-) specie, while in oxolation, metal centres are linked through oxo (-O-) bridge as follows.

$M\text{-}OH + M\text{-}OH_2 \rightarrow M\text{-}OH\text{-}M + H_2O$ (Olation, occurs for lower oxidation state cations)

$M\text{-}OH + H\text{-}OM \rightarrow M\text{-}O\text{-}M + H_2O$ (Oxolation, occurs for higher oxidation state cations)

For the deposition of thin films from above precursor solutions, two coating techniques are predominantly used, the dip coating and spin coating technique.

### 1.6.2 Dip Coating

Dip coating or immersion coating is a type of deposition technique, which results in deposition of thin films of desired coating material on a substrate. It is a simple, versatile, reliable, reproducible and cost-effective technique that enables the complex materials to be deposited easily. Dipping can be either automatic or manual .The batch dip coating process consists of five steps as shown in the figure 6 [48]. 1) Immersion, 2) withdrawal 3) deposition and drainage, 4) evaporation 5) curing/sintering. Dipping can be done either by using a dip-coater or can be done manually by keeping the speed constant and avoiding all the unnecessary vibrations. At first, the substrate is immersed with constant speed into the precursor solution to be coated. After a short delay, the process follows withdrawal of the substrate from precursor solution with same constant speed. The excess solution is drained from the substrate to the bath again leaving behind a thin coated film, followed by evaporation of solvent and drying of the film coated on the substrate. The film is subjected to curing step to undergo a chemical or physical change (if needed). Multi layered film can also be deposited by dipping the substrate into the same or different precursor solutions multiple times. Higher concentration of precursor solution results in agglomeration of nanoparticles on substrate surface.

The cohesive and adhesive forces between the substrate and precursor solution play a vital role in dip coating process. Strong cohesive forces between the precursor molecules cause weak interaction of liquid with the substrate during wetting process. On the other hand strong adhesive forces between liquid molecules and substrate surface result in stable thin film formation. Other forces like electrostatic and mechanical forces are also associated with dip coating technique.

Many factors like concentration and viscosity of the precursor solution, withdrawal speed of the film, immersion time and angle, temperature and evaporation rate affect the properties of deposited film. The withdrawal stage encounter several forces, one is called draining force which helps in draining of liquid from the substrate back to bath solution. Conversely, entraining forces help in retention of the fluid on the substrate surface. The thickness of coated film depends upon the balance between these two forces, a higher withdrawal speed produces thicker film [48]. Following equation is used to find the thickness of thin film.

$$h_0 = c(\frac{\eta U_0}{\rho g})^{\frac{1}{2}}$$

c = constant.

η = Viscosity.

$U_0$ = Rate of withdrawal speed of substrate from precursor solution.

P = density of the solution.

g = gravitational constant.

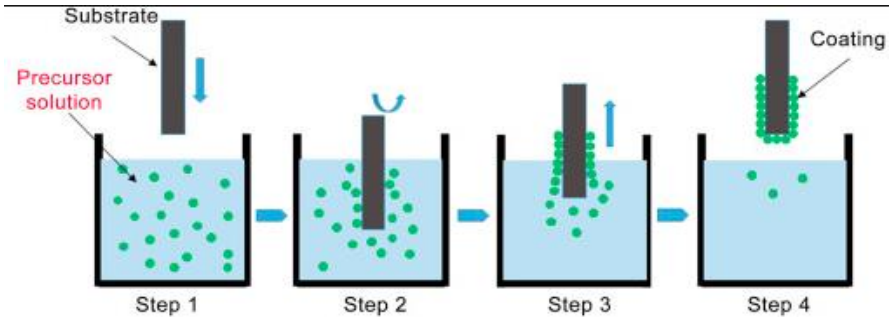


**Fig: 6 Schematic representation of multiple steps involved in dip coating technique.**

### 1.7 Electrochemical techniques

Electrochemistry deals with charge transfer processes related to chemical changes. This field includes the study of chemical changes occur due to passage of current and generation of electric energy from chemical energy. Electrochemistry has vast applications in different fields of technologies, few of them are devices like electrochemical batteries, fuel cells, electro-analytical sensors, electrochromic displays, metals electroplating, production of chlorine and aluminium on large scale and many more [49].

A typical electrochemical cell consists of three electrode system dipped in a suitable electrolyte solution, the working electrode, counter electrode (which act as cathode or anode according to nature the working electrode) and a reference electrode as shown in the figure 7. The supporting electrolyte increases the conductivity of the cell by providing the medium for charge transfer. Additionally, the supporting electrolyte controls the transfer of analyte to electrodes by three modes (convection, migration and diffusion). Mechanical forces like vibrations or stirring is used to move the analyte by convection mode. Ionic species are migrated to opposite electrodes by applying potential difference and diffusion occurs as a result of difference of concentration at two electrodes. The concentration of electrolyte can be used to reduce or increase the diffusion of analyte species to the electrodes.

Working electrode undergoes the process of interest. A potentiostat is connected to the cell to control applied potential of working electrode relative to the potential of reference electrode. The composition of working electrode varies from experiment to experiment and decides the potential window range. Reference electrode is one with stable and defined equilibrium potential, to which the potentials of other electrodes are compared and measured. Most commonly used reference electrodes are saturated calomel electrode (SCE), standard hydrogen electrode (SHE) and AgCl/Ag electrode. A porous frit is used to separate reference electrodes from the solution. After applying potential, the reaction (oxidation or reduction) occur at the working electrode results in flow of electrons and ions, a counter electrode is employed to complete this circuit. The counter electrode and the redox reaction products at counter electrode should be inert. Most commonly, a platinum wire or disk or carbon-based electrodes are used as a counter electrodes.

The cell is connected to an external power source (like potentiostat) to drive potential through the cell. The external circuit provides the path to the flow of electron, whereas, electrolyte solution provides medium to the flow of ions inside the cell. The load connected to external circuit utilizes the generated electrical power and completes the circuit [50].

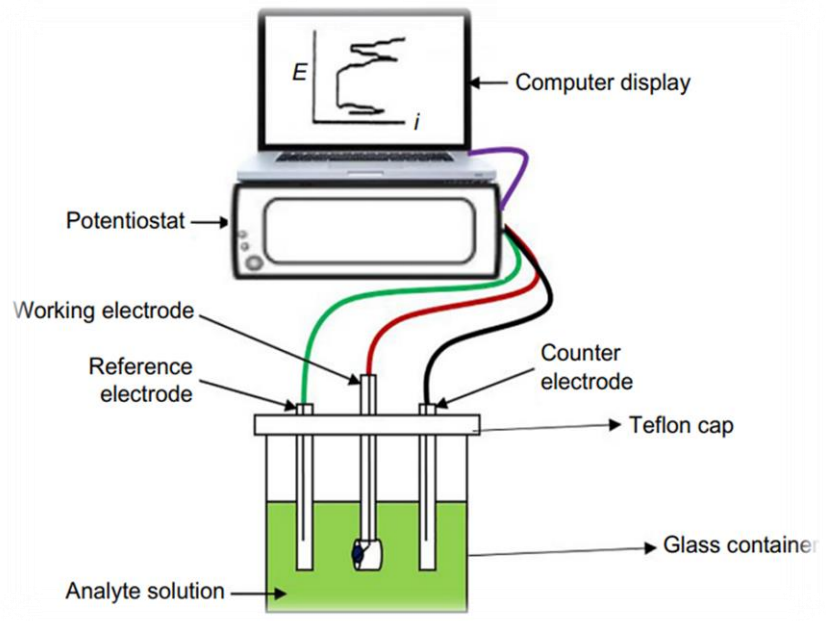


**Fig: 7 Three electrode based electrochemical fuel cell.**

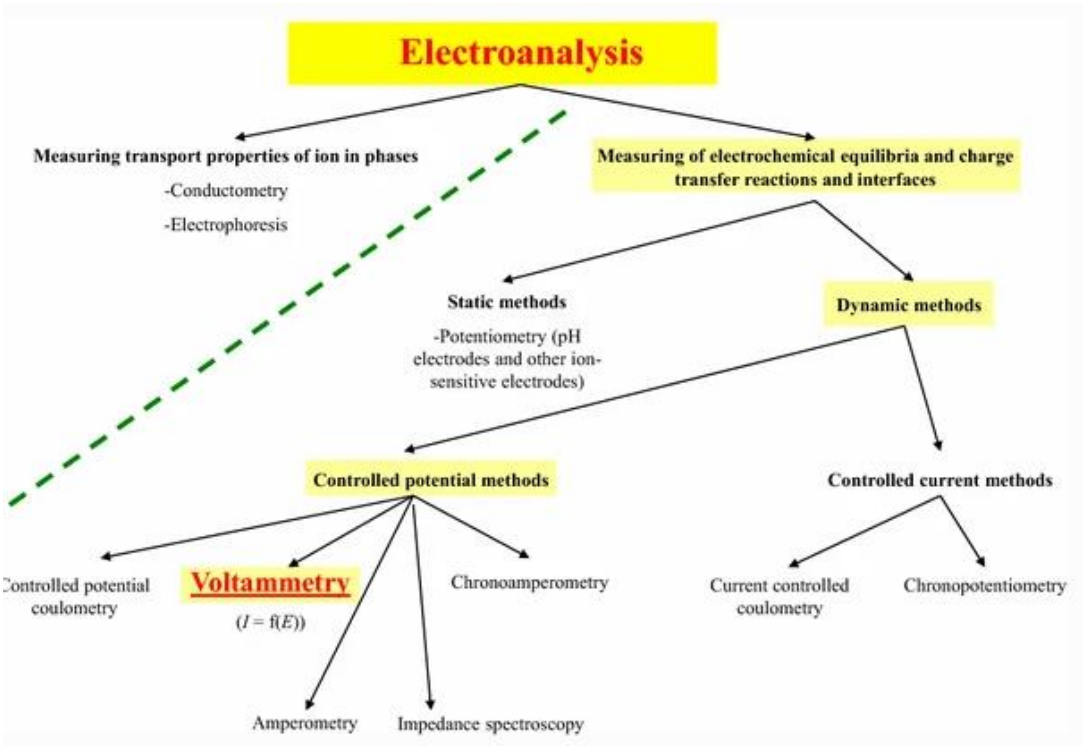


**Fig: 8 Schematic representation of types of electrochemical techniques.**

### 1.7.1 Cyclic Voltammetry (CV)

Cyclic voltammetry is very useful electrochemical technique, used to investigate the oxidation/reduction processes of the molecular species. A typical cyclic voltammogram displays current response of working electrode at y axis verses applied potential at x-axis. In the forward scan, potential is sweep from lower to higher value and current response of analyte is recorded called anodic trace, in the reverse scan potential is again sweep from higher value to lower value and current response of analyte is recorded called cathodic trace. The two peaks residing CV curve are associated with equilibrium of oxidized and reduced species and can be explained by Nernst equation. Nernst equation relates the electrochemical potential of the cell (E) to standard potential (E˚) and to other activities of oxidized/reduced species at equilibrium. Nernst equation provides understanding of electrochemical cell response to changes in potential and changes in concentration of redox species. In case of one-electro transfer reaction, the Nernst equation can be represented as follows,

$$E = E^{0\prime} + \frac{RT}{F}\ln\frac{[\mathrm{Fc}^+]}{[\mathrm{Fc}]} = E^{0\prime} + 2.3026\frac{RT}{F}\log_{10}\frac{[\mathrm{Fc}^+]}{[\mathrm{Fc}]}$$

E = electrochemical cell potential

E° = standard electrode potential

F = Faradays constant

R = Universal gas constant

T = Temperature

[$FC^+$] = oxidized form of analyte

[FC] = Reduced form of analyte

According to Nernst equation, for a reversible reduction reaction, first when potential is sweep cathodically from positive to negative value, the concentration of oxidized species ($FC^+$) decreases and the deposition of reduced specie (FC) occur at the working electrode (figure 8, point A to D). Diffusion of $FC^+$ from the solution, and its conversion to FC continues until an equilibrium is established between the two phases and highest reduction peak current is observed (figure 8, point C). The growing diffusion layer slow down the mass transfer rate of $FC^+$ species from the solution which ultimately decreases the current response

of working electrode (figure 8, point C to D). At point D the scan reverses, potential is sweep anodically from lower to higher and the deposited FC again oxidizes to $FC^+$ species. The concentration of oxidized specie at points B is equal to the concentration of reduced species at point E, following the Nernst equation, $E = E_{1/2}$ ($E_{1/2}$ corresponds to the potential difference between the two points C and F in figure 8). Hence, providing a way to estimate the $E^{0\prime}$ for the reversible redox reaction [50]. .

In case of irreversible electrochemical reactions, there is a high barrier to electron transfer which makes the kinetics of redox reactions sluggish and more negative potential is required for reduction, whereas oxidation reactions requires higher potential [51], [50].

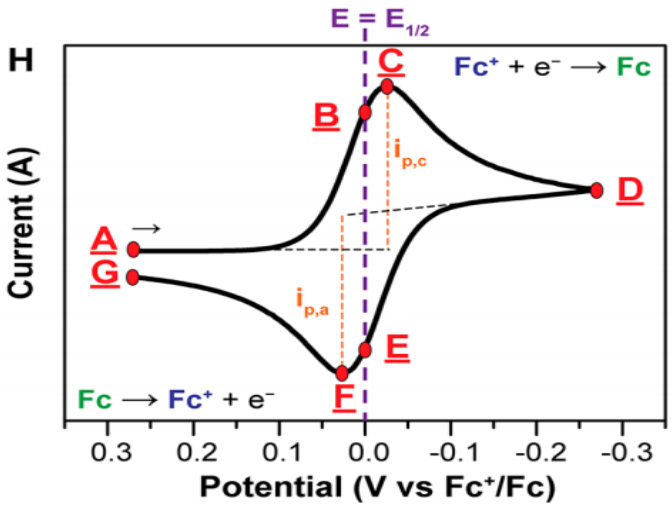


**Fig: 9 Cyclic Voltammogram of a reversible reduction reaction.**

### 1.7.2 Electrochemical Impedance spectroscopy

Electrochemical impedance spectroscopy (EIS) is a productive technique widely used for studying the dielectric and electrical properties of electrode-electrolyte interfaces. Till date EIS has been widely used for electrochemical characterization applications like determination of double layer capacity, diagnosis of metal corrosion, characterizing electrodeposition of different materials, study of electrical properties of interfaces and materials, electro-organo synthesis and the diagnosis of fuel cells [21-27]. EIS can be used for two types of measurements, ex situ and in situ measurements. Ex situ measurements diagnose properties of different materials and cell components, hence provide information for designing a fuel cell. In situ measurements provide information regarding operating conditions and help in designing a fuel cell with optimized operating conditions [52].

In EIS measurements a small AC amplitude signal (voltage or current signal) with voltage/current value equal to that of 1–5% of DC voltage/current, is applied to DC voltage or current with a frequency range (0.001–36,000,000 Hz) and impedance response of the cell is recorded by the EIS instrument as Bode plot or Nyquist plot. The Nyquist plot displays plot of imaginary impedance/resistance vs real impedance /resistance as shown in figure 9, whereas, Bode plot as shown in figure 10, displays resistance vs phase angle as a function of frequency. [52].

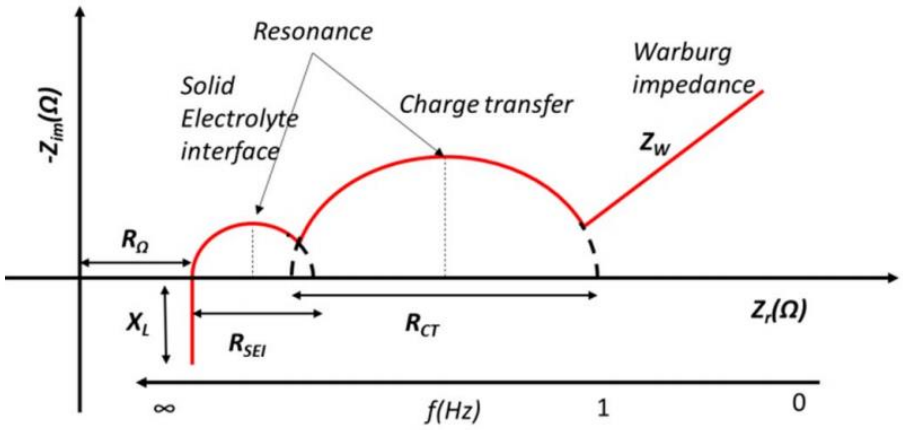


**Fig: 10 Nyquist plot**

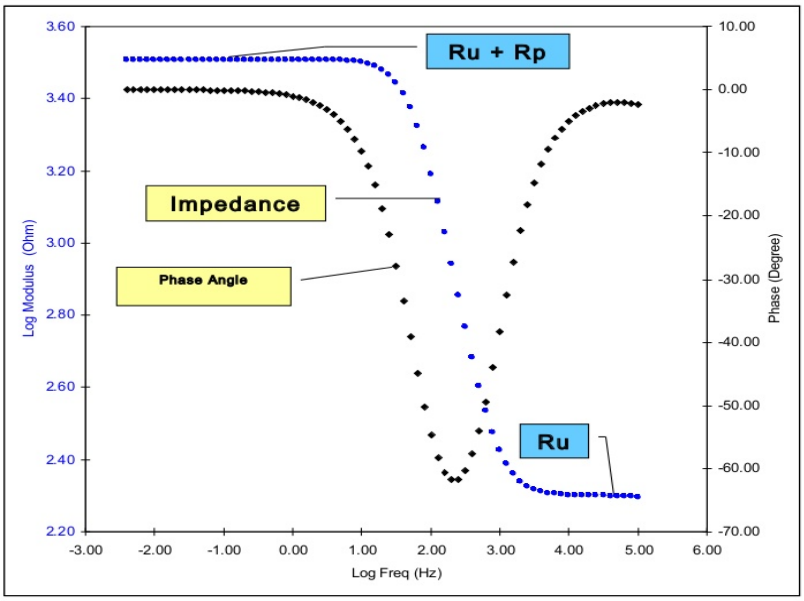


**Fig: 11 Bode plot**

Impedance of electrochemical systems is determined by using ohm's law. The EIS data can be interpreted by comparing the EIS spectrum to an equivalent circuit called Randle circuit as

shown in figure 11. ZSimpWin software can also be used to analyse the spectrum by equivalent circuit fitting [53]. Equivalent circuits are designed according to the shape of EIS spectrum obtained, usually consists of conductors (C), resistors (R) and capacitors (C), connected in a series or parallel. The Nyquist plot exhibits two regions of high frequency and low frequency. The semicircle in the high frequency region gives information about the charge transfer resistance (Rct) at the electrode-electrolyte interface, whereas, the Warburg impedance which is defined as resistance to ions diffusion from electrolyte to the electrode material is responsible for the straight line behaviour in the Nyquist plot in the low frequency region [54]. Both Zw and Rct together are called polarization resistance (Rp).

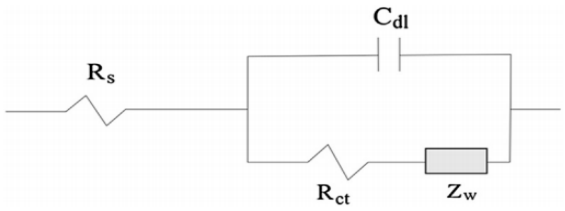


Electrolyte solution resistance (Rs),
Double-layer capacitance (Cdl),
Charge transfer resistance (Rct) and the
Warburg impedance (Zw).

**Fig: 12 Randle circuit**

### 1.7.3 Chronoamperometry

Chronoamperometry (CA) is another powerful electrochemical technique used to study the kinetics of diffusion processes, chemical reactions and adsorption phenomena. In this technique a constant potential is applied to the system and current response of the analyte is measured as function of time. CA has been used for detection of analyte in the flow system, studying the electrochemical activity of analytes, stability of electrocatalysts and sensing application. At first, the potential is kept at value where no faradaic process occurs at the electrode, then the input potential is stepped to a value at which the oxidation/reduction reaction occurs and the concentration of electro-active analyte species become zero, which results in current decay. At zero time the potential start stepping up. For diffusion-controlled processes, current decays with the inverse square root of time as shown in the figure 12 below [55]. CA works on the principle of Cottrell's equation.

$$i(t) = nFAC\sqrt{\left(\frac{D}{\pi t}\right)} = \frac{k}{\sqrt{t}}$$

n = number of electrons, F = Faraday constant,

A = surface area of the electrode, C = concentration of analyte

D = diffusion coefficient of analyte, t = time, i = current

By using chronoamperometry, all the variables in Cottrell's equation can be calculated as long as the other variables are known. The Cottrell equation foretell the variation of current with time and is valid only incase of diffusion current arrived from diffusion of analyte species to the electrode surface, hence the solution should not be stirred [54]. The current-time plot basically reflects the change in concentration gradient in the neighbourhood of the electrode surface.

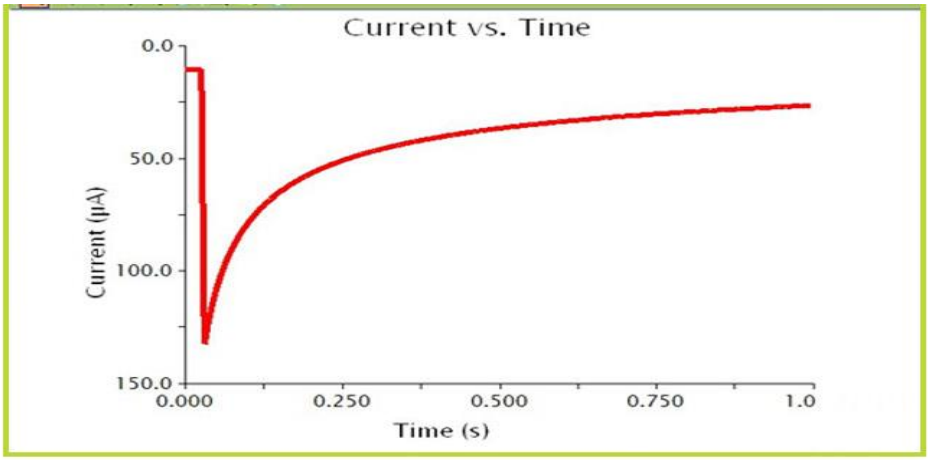


**Fig: 13 Chronoamperogram**

## 1.8 Characterization techniques

### 1.8.1 X-ray Diffraction (XRD)

X-ray diffraction is a non-destructive characterization technique used to study the properties of crystalline materials, since the wavelength range of x-rays (0.2-10 nm) is comparable to that of interatomic spacing in crystalline materials. This technique helps in identification of crystalline materials by measuring the average spacing between atomic rows in a crystal lattice, determines the orientation of single crystal, sample purity, phase of the material, crystal defects and measure the average shape and size of small crystalline regions[56].

As each crystalline material has a unique lattice and atomic structure, irradiated collimated beam of X-rays is scattered due to interaction of photons with the electrons of the sample material. The scattered beams undergo constructive or destructive interference which generate unique diffraction patterns consisting Bragg diffraction peaks. By comparing these patterns of diffraction with reference spectra, specific crystalline phase of sample material can be identified. Bragg's law describes the relation between interatomic spacing of sample material and wavelength of X-ray beam and is given by following equation;

$$2d\sin\theta = n\lambda$$

d = perpendicular distance between adjacent planes

θ = Bragg angle

λ = wavelength of X-ray beam

n = order of the reflection

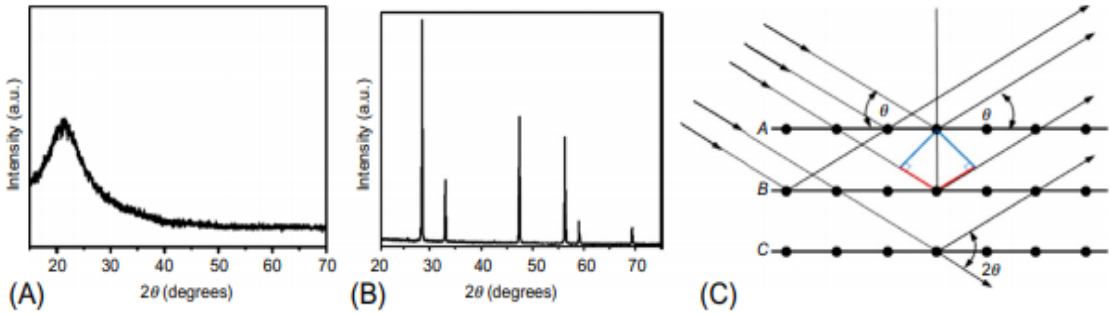


**Fig: 14 XRD patterns of (A) amorphous (B) crystalline and (C) reflection of X-ray beam with specific angle from adjacent planes within the crystal.**

### 1.8.2 Scanning electron microscopy

SEM is basically a surface imaging technique which uses an electron beam to produce high resolution and highly magnified images of sample material by scanning its surface. SEM can produce images with resolution up to 1 nm and magnification up to 400,000x. [57]. The incident electron beam, carrying negative charge, interacts with sample material that constitutes a specific order of atoms and electronic cloud, which produces specific signals presenting the topographic details and composition of scanned surface [56]. On interaction with the sample, high energy electron beam causes emission of secondary electrons (Se) from the surface atoms, back-scattered electrons (BSE) called primary electrons as a result of elastic

scattering, auger electrons and emission of characteristic X-rays from inner shells of the surface atoms. All these carry different information regarding sample and are detected using specific detectors. Primary electrons carry information about composition, secondary electrons are very important, the signal generated from them produces a high resolution image, revealing the surface topography of the sample. The characteristic X-rays produced are used in energy dispersive x-ray analysis (EDX) [56].

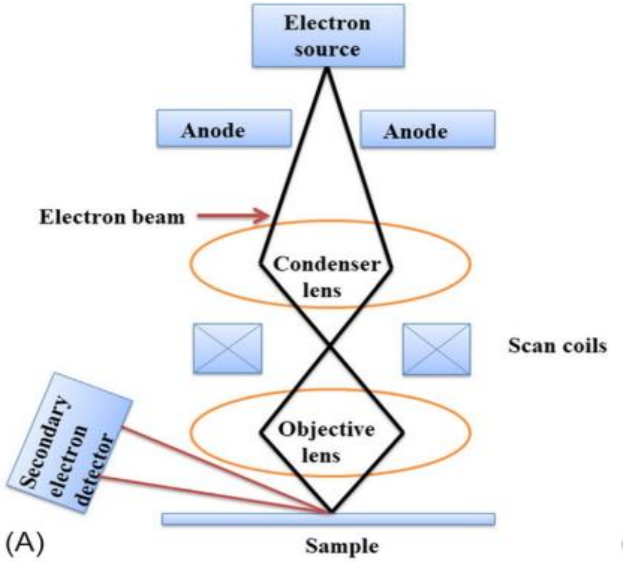


**Fig: 15 schematic representation of scanning electron microscope**

The (EDS) technique is used in combination with SEM technique. The emitted X-rays from sample surface carry valuable information about elemental surface composition. Thus, SEM imaging coupled with EDS elemental mapping can provide both chemical and physical information about the sample[56].

### 1.8.3 Raman spectroscopy

Raman spectroscopic technique works on the principle of scattering of light. It basically gives information about vibrational and other lower modes of frequency which help in molecular identification. When light from a monochromatic laser light source interacts with solid, liquid or gaseous sample, majority of the photons are scattered elastically with the same energy as incident photons, called Rayleigh scattering. A small number of incident photons are scattered with energy different from the incidents photons, called inelastic or Raman

scattering. The information about the vibrational signature of the molecule is obtained from that shift in energy. After scattering phenomenon, the sample molecule is in a different vibrational or rotational state, if its energy is higher than its initial state then the energy and hence frequency of the scattered photon will be less than the incident photon, this shift in frequency is termed as strokes shift. If the final state energy of the sample molecule is less than the initial state then the photon will be scattered with higher energy/frequency. This frequency shift is called Anti-stokes shift.

In order for a molecule to be Raman active, it must have a change in its polarizibility attributed to a change in shape, size or orientation of the electronic cloud surrounding the molecule, unlike IR spectroscopy which is observe change in electric dipole moments of the molecules.

### 1.9 Challenges

Although tremendous amount of research work has been done to improve the overall performance of direct methanol fuel cells to be used as alternatives for energy production, still the DMFCs are associated with unavoidable problems which hinder their commercialization. The major challenges faced with the use DMFCs are follows;

• At anode catalyst, uniform distribution of methanol concentration is highly required for better performance of the cell. High methanol concentration causes (1) increase in methanol cross-over which causes cathode over-potential (2) decrease mass transport loss which enhances cell performance (3) increases cell temperature due to oxidation of crossed-over methanol at the cathode, ultimately improving the electrochemical performance of the cell. Reportedly, the optimum methanol feed concentration for enhanced cell performance is 2 to 4 M. Decrease/increase in methanol feed concentration from this range affects cell performance [58].

• Likewise, at anode catalyst sufficient availability and uniform distribution of water is necessary for efficient cell performance. Insufficient availability of water leads to incomplete oxidation of methanol and formation of toxic intermediates like formaldehyde, therefore sufficiently diluted methanol feed is used. Excess water may cause cathode water flooding by blocking the pores of diffusion layer and hinder oxygen transport. Flooding problem can be tackled by controlling water/methanol cross-over and promoting water back flow.

• The carbon dioxide produced at anode as a result of electrochemical reaction may get accumulated on anode catalyst layer and reduces the available active sites for methanol oxidation. It may cause blockage of the pores of anode diffusion layer and terminates methanol diffusion, which ultimately decrement the overall cell performance. Therefore, the continuous removal of carbon dioxide is necessary [59].

• Proper heat management is necessary while operating DMFC to minimize heat loss and keep the temperature sufficiently high for improving electrochemical reaction kinetics at both the electrodes and boost the overall cell performance. At anode, overpotential generates heat which is used in electrochemical reaction, while at cathode heat is generated by overpotential, oxidation of crossed-over methanol and electrochemical reaction at cathode, which is consumed in water evaporation.

• One of the major problems associated with DMFCs is methanol cross over issue. Methanol diffuses from high concentration at anode to lower concentration at cathode through PEM. At cathode the crossovered methanol is directly oxidized by the oxygen present which results in mixed potential and loss of cell voltage. Methanol cross-over also causes poisoning of cathode catalyst and electrolyte membrane. It is also responsible for water flooding at cathode. Methanol cross over can be controlled by maintaining the concentration of methanol feed low, using highly active catalysts for methanol oxidation, use of thicker electrolyte membranes and using methanol-inert cathode catalysts [60].

• The sluggish reaction kinetics of the methanol oxidation reaction is still a major challenge faced with the use of DMFC. Development of highly active nano-sized uniformly distributed electro-catalysts can improve anode kinetics.

• For commercial feasibility, the durability and stability of a fuel cell are key requirements. The fuel cell may encounter permanent performance decay due degradation of its components like electro-catalyst, electrolyte membrane and current collector. The reversible performance decay (can be recovered after cell operation) is caused by factors like carbon dioxide accumulation at anode, cathode water flooding etc. Significant amount of studies have been done to improve the life time and stability of DMFCs.

• Another main obstacle in the way of commercializing DMFCs is their high cost. Main contributors to its high cost are expansive platinum catalysts, Nafion membranes and noble metals coating on current collectors. High cost problem has been largely resolved by using

in-expansive non-noble metal based electro-catalysts as alternative to expansive noble metal catalysts [61].

# CHAPTER 02

## Literature Review

1) M.A Mansoor and co-workers fabricated flower like $MnZnO_3$ thin films via AACVD technique. The photoelectrochemical performance of prepared films was observed for oxidation of methanol using Ag/AgCl as reference electrode, Pt as counter electrode in 0.5M electrolyte solution of NaOH. The $MnZnO_3$ photoanode showed enhanced photocurrent density (3 times higher than pure NaOH) with addition of 0.6M methanol at 0.0V in the presence of light. Additionally, chronoamperometric analysis showed the stability of thin films on addition of methanol towards corrosion in basic medium. Impedance spectroscopy revealed a decrease in electron transfer resistance (Rct) (from 702 to 395.5) with 0.6M methanol addition which indicates good charge-transfer and enhanced current density [62].

2) K. Munawar et al deposited thin films of trimetallic oxide composite ($CuO–MnO–2TiO_2$) on FTO-glass via AACVD technique. Fabrication of trimetallic composite induces synergic effect which decreases electron-hole recombination and enhances charge transfer which ultimately improves the photoelectrochemical performance of prepared film. Photoelectrochemical performance of prepared films was evaluated in dark and under light irradiations using LSV technique. Under sunlight irradiation 2.21 mA of photocurrent density was observed at 0.7 V in 0.5 M $Na_2SO_4$ electrolyte solution with respect to Ag/AgCl reference electrode at scan rate of 50 mV/s[63].

3) M.A Mansoor et al. in another study fabricated FTO-glass deposited thin films of $CeO_2$–MnO composite (Ce:Mn ; 1:9) by AACVD technique. Different characterization techniques and electrochemical studies revealed that morphology and photocurrent of the prepared films is highly dependent on deposition temperature, under light irradiation a maximum photocurrent density of 265 μA $cm^{-2}$ at 0.65 V was observed with films deposited at 475 °C for 45 min, in 0.5M sodium hydroxide electrolyte solution using Ag/AgCl/3M KCl as reference electrode[64].

4) M.A Mansoor and team synthesized FTO-glass deposited $Mn_2O_3$-$TiO_2$ composite thin films (Mn:Ti ; 1:2) from trinuclear bimetallic complex precursor at different temperatures (400,450,500,550) by AACVD technique. UV spectroscopic analysis revealed decreased band gap energies of prepared films compared to reported values, owing to synergic effect which facilitates migration of electrons from conduction band of $MnO_3$ to $TiO_2$ and trapping

holes, ultimately enhancing the charge separation efficiency and photoelectrochemical performance of the prepared films. Different characterization techniques and electrochemical studies revealed that morphology and photocurrent of the prepared films is highly dependent on deposition temperature, under light irradiation a maximum photocurrent density of 1.3 mA $cm^{-2}$ at 0.65 V was observed with films deposited at 500 °C, in 0.5M aqueous $Na_2SO_4$ electrolyte solution using Ag/AgCl/3M KCl as reference electrode. Results proved that prepared films are best photoelectrodes for photoelectrochemical applications[65].

5) A Saroni et al. presented heterojunction thin films deposited on $In_2O_3$ coated c-silicon substrate using $N_2$ plasma-assisted in-situ annealing approach. Linear sweep voltametric analysis of $WO_3/In_2O_3$, $W_2N/In_2O_3$ and $InN/In_2O_3$ films showed enhanced current density value of 0.429, 1.84 and 0.966 mA/$cm^2$ vs. Ag/ AgCl reference electrode at potential of 1 V, compared to bare $In_2O_3$ thin films. The enhancement of photocurrent was attributed to synergic effect aroused from electronic interaction between films of semiconductors which helped in decreasing the band gap energy, enhancing electron-hole separation efficiency, enhanced visible range absorption and improved photoelectrochemical properties of the heterojunctions[66].

6) K. Munawar and co-workers fabricated FTO-glass coated $Ca_2Mn_3O_8$-CaO composite thin films via AACVD technique at different temperatures (450, 500 and 550 $^0$C). Different characterization techniques revealed successful formation of porous, textured thin films. Under light illumination, among prepared films highest photocurrent density of value 3.75 mA $cm^{-2}$ was observed with films deposited at 500 $^0$C at potential of 0.8 V using SCE as reference electrode. The decreased band gap energy and enhanced photoelectrochemical performance of $Ca_2Mn_3O_8$-CaO composite films was attributed to synergic effect which increases photo absorption ability and improve electron-hole transfer mechanism between mixed semiconductors[67].

7) S.Ahmed and team deposited $CuYO_2$–$0.5Cu_2O$ composite thin films (Cu:Y ; 2:0.95) on FTO-glass from copper-yttrium hexanuclear complex precursor in argon environment at 400 $^0$C via AACVD. Synthesized complex precursor was characterized using FT–IR, TG/DTG, melting point, XRD and elemental analysis techniques. Characterization techniques, SEM and EDX showed successful formation of pure and crystalline $CuYO_2$–$0.5Cu_2O$ composite thin films with uniformly distributed granules of $CuYO_2$ (110 – 125 nm) and $Cu_2O$ rods (0.85

– 1.05 μm). Linear sweep voltammogram showed a photocurrent density of 81 μAcm$^{-2}$ at potential of 1.0 V using SCE as standard electrode under light irradiation[68].

8) M.A.Ahsan et al. and co-workers synthesized single source precursor complex for deposition of CuO–1.5$ZrO_2$ composite thin films on FTO glass at 500 $^0$C by using AACVD technique. The synthesized complex was characterized by TG/DTG and DSC analytical techniques. Successful formation of ultra-pure microspherical CuO–1.5$ZrO_2$ composite thin films was confirmed by different characterization techniques. The electrochemical performance of prepared film was investigated via cyclic voltammetry by oxidation of methanol in alkaline medium, oxidation peak current of 14 μA was recorded which was 3.5 times to that of bare Pt electrode[69].

9) Che Mat et al. fabricated Anatase-supported $MnO_2$- $RuO_2$-$Co_3O_4$ (13:1:13 ratio) composite via simple precipitation and PEC performance of prepared photocatalyst was investigated by cyclic voltammetry and EIS studies for oxidation of methanol in 0.1 M KOH electrolyte solution under visible light irradiation. Maximum current value of 0.37 mA cm$^{-2}$ was recorded on addition of 4 M methanol compared to Pt/C electrode which gave peak current value of 0.54 mA cm$^{-2}$ on oxidation of 3M methanol, this enhancement of photocurrent was attributed to enhanced charge migration and separation efficiencies under visible light irradiation. It was also reported that decrease in band gap energy (1.66 eV) of trimetallic supported Anatase was due to formation of oxygen vacancies by diffusion of Mn, Ru and CO to the lattice of Anatase. Overall results concluded that the prepared trimetallic anatase composite is best for direct methanol fuel cells application[70].

10) S.Mehmood and team synthesized rGO-$Co_3O_4$ nanocubes via hydrothermal technique. The electroctalytic performance of prepared nanocubes towards methanol oxidation was investigated by CV and EIS using different weight % of graphene oxide. A maximum oxidation peak current of 362 μA/cm$^2$ was recorded with rGO-$Co_3O_4$ nanocubes modified electrode with 2% by weight graphene oxide content. Furthermore, the prepared composite electrode showed good stability and reversibility towards oxidation of methanol. Low cost, facile fabrication methodology and good electrocatalytic performance proved that prepared metal oxide-GO composite could be used as best ulternative electrodes in direct methanol fuel cells[71].

11) Pie Lim et al. deposited silver on $TiO_2$-deposited ITO-glass substrate by sonochemical method. The photoelectrocatalytic behaviour of prepared Ag-$TiO_2$ electrode was investigated

towards oxidation of methanol in 0.1 M $Na_2SO_4$ electrolyte solution using Ag/AgCl as reference electrode, a maximum photocurrent density of 1 mA/cm$^2$ was recorded which was 4 times to that of bare $TiO_2$ electrode. This enhancement of photocurrent was attributed to Ag acting as electron sink leading to suppression of electron-hole recombination and improved charge transfer efficiency. Furthermore, DFT calculations revealed that efficient adsorption of methanol on Ag surface and charge transfer from Ag to methanol[72].

12) Chen and co-workers synthesized platinum nanoparticles decorated rugged Ni films via pulse electrodepositon technique. Electrocatalytic performance of prepared Pt/Karst-Ni films towards methanol oxidation in 1M KOH electrolyte solution at scan rate of 20 mV/s was evaluated through cyclic voltammetry. XPS analysis confirmed presence of $Ni(OH)_2$ on Ni surface which enhances CO tolerance of platinum electrocatalyst, ultimately making the electrocatalytic performance more efficient. Decrease in binding energy was also noticed owing to charge transfer from Ni to platinum (synergic effect). Prepared Pt/Karst-Ni films showed enhanced electrocatalytic reduction of methanol compared to bare pt and pt/Ni electrode[73].

13) K.V.Ozdokur et al. fabricated $TiO_2$/ZnO/Pt nanocomposite via DC sputtering followed by electrodeposition of prepared nanocomposite on FTO glass. Cyclic voltammograms of prepared films revealed enhanced catalytic performance towards oxidation of methanol compared to bare FTO/$TiO_2$/Pt and FTO/Pt attributed to synergic effect due to electronic interaction between mixed metal oxides and platinum[74].

14) Jiang and co-workers presented two types of Pt−Ru films, one was fabricated by co-deposition of Pt-Ru with different ruthenium content via atomic layer deposition technique and another one was Pt skin catalyst fabricated by deposition of porous layers of platinum of varying thickness on ruthenium films via ALD. The electrochemical performance of prepared films for methanol oxidation was investigated through CA and CV analysis (in 0.5 M $H_2SO_4$/16.6 M $CH_3OH$ at 0.1 V/s). Co-deposited catalysts with (Pt:Ru 1:1) composition showed highest catalytic activity compared to bare platinum and Pt skin catalyst. Additionally, the electrocatalytic performance of sputtered ruthenium in Pt skin catalyst was enhanced by platinum layer deposition[75],

15) J Hoseini et al. fabricated Pt/Fe/$Fe_2O_3$ nanohybrid ultrathin films from toluene-water interface medium. Prepared films showed high CO tolerance and electrocatalytic performance towards methanol oxidation among other tested electrocatalysts. Ratio of

maximum current density in forward scan to maximum current density in reverse scan ($j_f/j_b$) for the prepared thin films was calculated about 8.09 higher than that of commercial platinum. Higher $j_f/j_b$ ratio corresponds to complete oxidation of methanol and high CO tolerance, this higher $j_f/j_b$ value was attributed to presence of $Fe_2O_3$ which acted as active oxygen provider to the adsorbed residues of methanol (CO) on Pt surface and facilitating its conversion to $CO_2$[76].

# CHAPTER 03

# EXPERIMENTAL

## 3.1 Materials

Following chemicals used in the fabrication of NiO-$Y_2O_3$/FTO and NiO-$ZrO_2$/FTO composite thin films were analytical grade and were used as received. Nickel(II) acetate dihydrate [$Ni(CH_3CO_2)_2.2H_2O$, sigma Aldrich], zirconium(IV) acetate [anhydrous, $Zr(CH_3COO)_4$ sigma aldrich], yttrium(III) acetate hydrate [$Y(CH_3COO)_3.H_2O$, Sigma Aldrich], sodium hydroxide [NaOH, Sigma Aldrich], methanol [99.8% Sigma Aldrich], ethanol [99.8% Sigma Aldrich], trifluoroacetic acid [TFA, Sigma Aldrich] and commercially available fluorine tin oxide coated glass [FTO, Sigma Aldrich]. Deionized water was used throughout the experimental analysis.

## 3.2 Instruments

Digital weight balance, magnetic stirrer with hot plate, heating oven, muffle furnace, ultrasonication bath and electrochemical potentiostat. The topography of the prepared thin films was characterized by SEM (TESCAN) with magnification ranging upto 100,000 x. For elemental mapping EDS was conducted (Oxford Instrument INCAx-act PentaFET Precision). The crystallinity of the films was revealed via XRD (Bruker D8 Advance, Germany) with 2θ range from 10° to 90° and at 1.54A˚ wavelength of Cu Kα radiations. X-ray photoelectron spectroscopy (XPS) (Versa probe II, ULVAC-PHI, Inc. Chanhassen, MN, USA) studies were conducted under an ultra-high vacuum (~$10^{-10}$ mbar). The synthesis of thin films was further confirmed by FTIR (Bruker Alpha, platinum ATR) with spectral range of 4000 to 500 $cm^{-1}$ and Raman (Nikon, eclipse ci) spectroscopic analysis.

## 3.3 Methodology

### 3.3.1 Preparation of precursor's solutions

To prepare 0.1M of nickel acetate, zirconium acetate and yttrium acetate solutions, known amounts of $Ni(OAc)_2.2H_2O$, $Zr(CH_3COO)_4$, $Y(CH_3COO)_3.H_2O$ salts were dissolved in methanol upon stirring at room temperature, few drops of TFA were added to yttrium acetate solution to completely solubilize it in methanol. Then to prepare 1:1 precursor solutions for (NiO-$ZrO_2$) and (NiO-$Y_2O_3$) thin film deposition, known volumes of prepared 0.1M salt solutions were mixed upon stirring at room temperature as shown in the figure 16. For

comparative study solutions of different molarities and ratios were also prepared via same route.

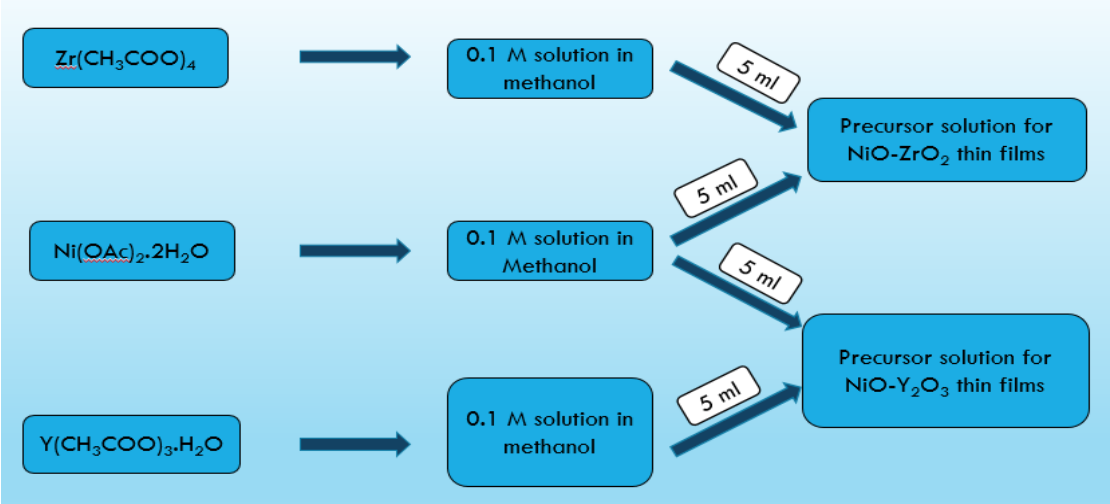


**Fig; 16. Preparation of precursor solutions.**

### 3.3.2 Fabrication of metal oxide composite (NiO-$ZrO_2$/FTO) thin films

NiO-$ZrO_2$ thin films were deposited on FTO-glass substrate by dip coating method. FTO glass was cut into dimensions 2×1$cm^2$ (l×w). Before deposition FTO substrate was washed thoroughly with a mixture of acetone and ethanol solvents and sonicated for about 15 minutes at room temperature using ultrasonication water bath. After washing and drying at room temperature the FTO substrate was dipped in 0.1 M precursor solution of Ni-Zr mixture for 45 seconds and then dried on hot plate for 10 minutes at 100$^o$C. After deposition of first layer of thin film, same film was dipped again in the precursor solution for 45 seconds for the deposition of second coating of thin film followed by drying on hot plate for 10 minutes at 100$^o$C. Same procedure was repeated ten times to produce uniform and ultrathin films coated FTO. After deposition the prepared films were calcined at 500$^0$C for 3 hours in a muffle furnace. Same procedure was employed to fabricate nickel oxide and zirconium oxide thin films separately for comparison purposes.

### 3.3.3 Fabrication of metal oxide composite (NiO-$Y_2O_3$/FTO) thin films

NiO-$Y_2O_3$ thin films were also deposited on FTO-glass substrate by dip coating method as explained above. FTO glass was cut into dimensions 2×1$cm^2$ (l×w). Before deposition FTO substrate was washed thoroughly with a mixture of acetone and ethanol solvents and sonicated for about 30 minutes at room temperature using ultrasonication water bath. After washing and drying at room temperature the FTO substrate was dipped in 0.1 M precursor

solution of Ni-Y mixture for 45 seconds and then dried on hot plate for 10 minutes at 100$^{o}$C. After deposition of first layer of thin film, same film was dipped again in the precursor solution for 45 seconds for the deposition of second coating of thin film followed by drying on hot plate for 10 minutes at 100$^{o}$C. Same procedure was repeated ten times to produce uniform and ultrathin films coated FTO. After deposition the prepared films were calcined at 500$^{0}$C for 3 hours in a muffle furnace. Same procedure was employed to fabricate nickel oxide and yttrium oxide thin films separately for comparison purposes.

Schematic representation of metal oxide composite thin films synthesis via dip coating method is presented in Fig; 17.

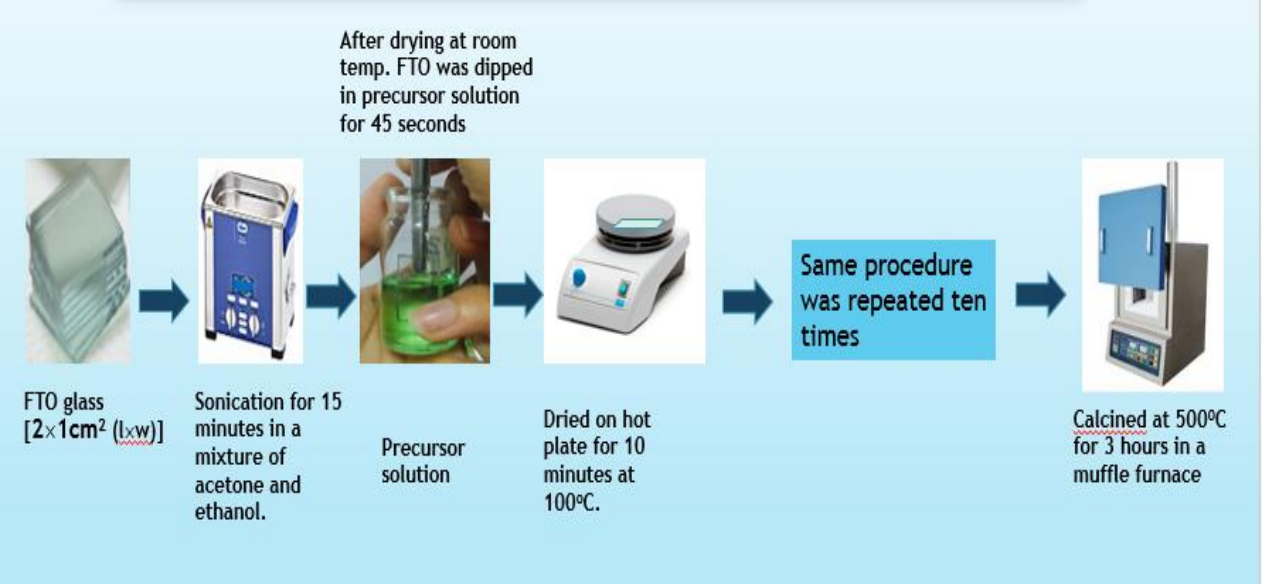


**Fig; 17. Schematic representation of metal oxide composite thin films synthesis via dip coating method**

### 3.3.4 Electrochemical oxidation of methanol via prepared metal oxide thin films

Electrocatalytic behaviour of prepared thin films towards methanol oxidation was studied using electrochemical potentiostat (Reference 3000 potentiostat/galvanostat/ZRA by Gamry consisting of three electrode system as shown in figure 18. The study was carried out in 0.5M NaOH electrolyte solution at scan rate of 100 mV/s, using Pt wire as counter electrode, Ag/AgCl as reference electrode and prepared metal oxide composite thin film as working electrode, providing potential range of -0.5 to 2.0V. All the three electrodes were dipped in the electrolyte solution and catalytic behaviour of fabricated thin films was investigated by recording voltammograms at 100 mV/s before and after addition of (0.2, 0.4, 0.6, 0.8, and 1M) methanol to the reaction medium. Cyclic voltammetry (CV), electrochemical impedance

spectroscopy (EIS), chronoamperometry (CA) studies were performed to evaluate the efficiency of prepared metal oxide thin films for methanol oxidation. Furthermore, effect of scan rate and concentration precursor solution thin on methanol oxidation process was also studied using same experimental parameters.

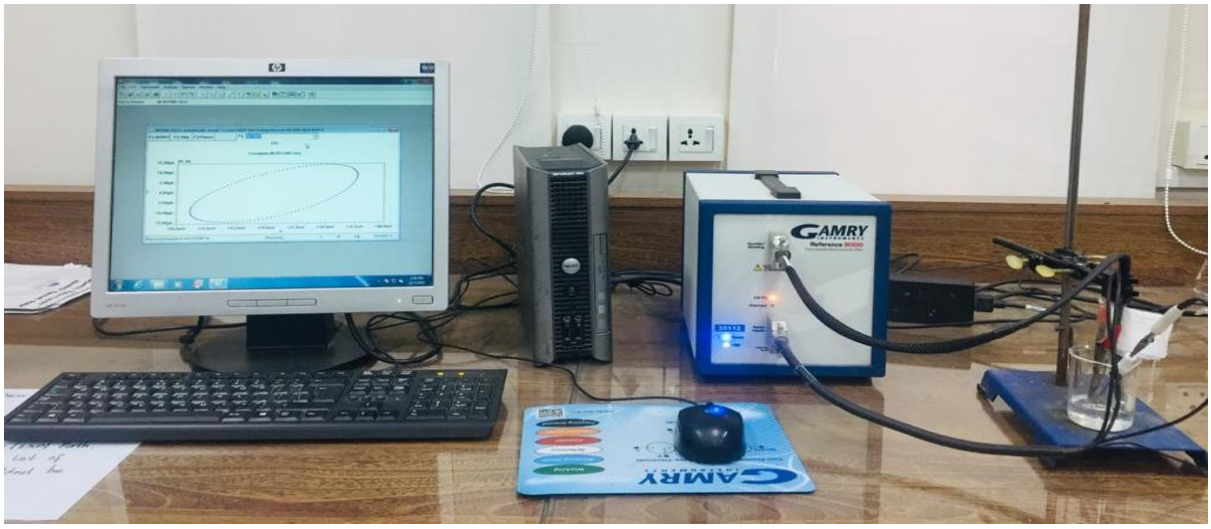


**Fig; 18 Three-electrode based electrochemical setup**

**CHAPTER 04**

# Results and Discussion

## 4.1 Characterization of (NiO-$ZrO_2$/FTO) and (NiO-$Y_2O_3$/FTO) thin films

### 4.1.1 SEM analysis

The morphology and textural features of the prepared metal oxide thin films were analysed via SEM. Figure 19 shows SEM images of NiO, $ZrO_2$ and NiO-$ZrO_2$/FTO. SEM images revealed that the prepared thin films constitute porous layers of well-interconnected uniformly distributed irregular-shaped stacks of particles. The average particle size of $ZrO_2$ and NiO-$ZrO_2$/FTO metal oxide thin film was calculated to be 230 and 180 nm respectively. Figure 20 display SEM images of $Y_2O_3$ and NiO-$Y_2O_3$/FTO thin films. $Y_2O_3$ shows porous surface with uniformly distributed and well-interconnected irregular-shaped particles of calculated average size of 121 nm. SEM images of NiO-$Y_2O_3$/FTO thin film revealed the formation of smooth and uniform porous layer. The characteristic well connected particles and porosity of the surfaces allow the methanol and electrolyte solution to diffuse to the deeper layers of the prepared catalyst which ultimately boost the MOR kinetics and efficiency.

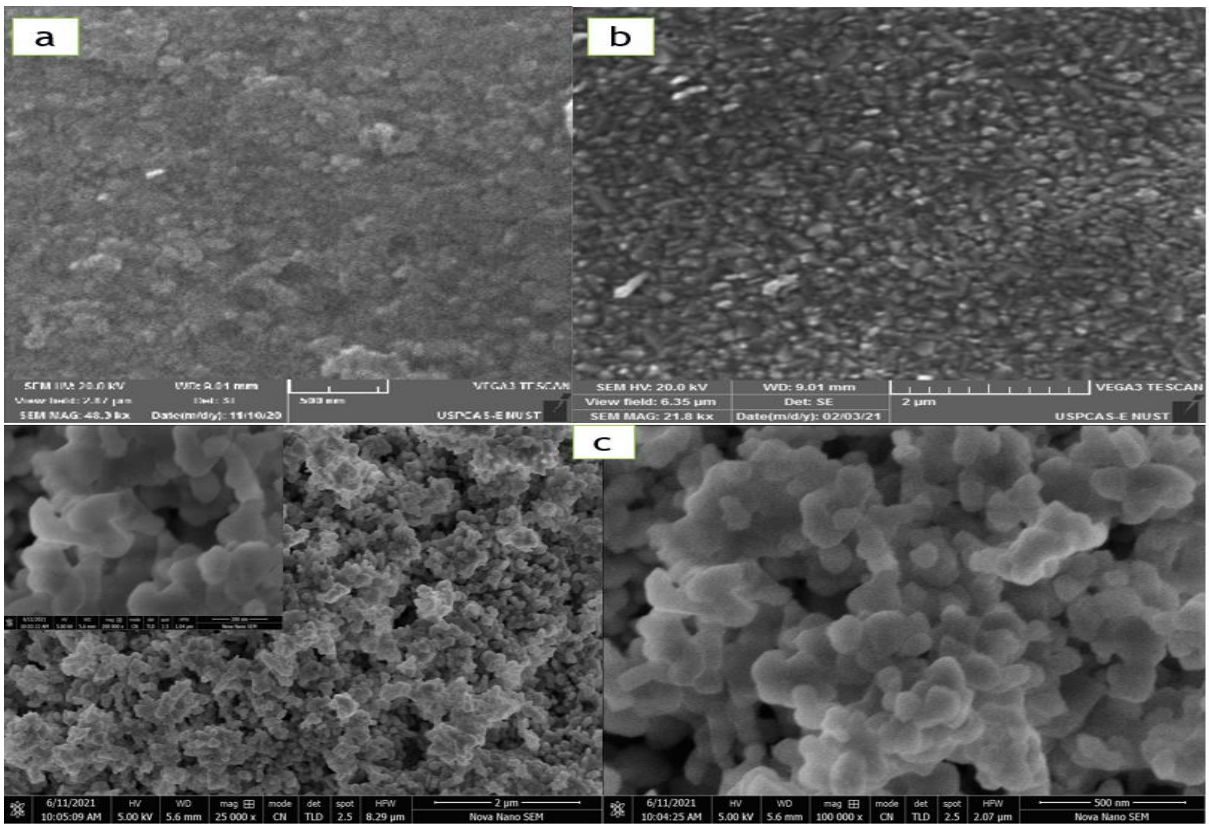

**Fig; 19. SEM images of a) NiO b) $ZrO_2$ and c) NiO-$ZrO_2$/FTO**

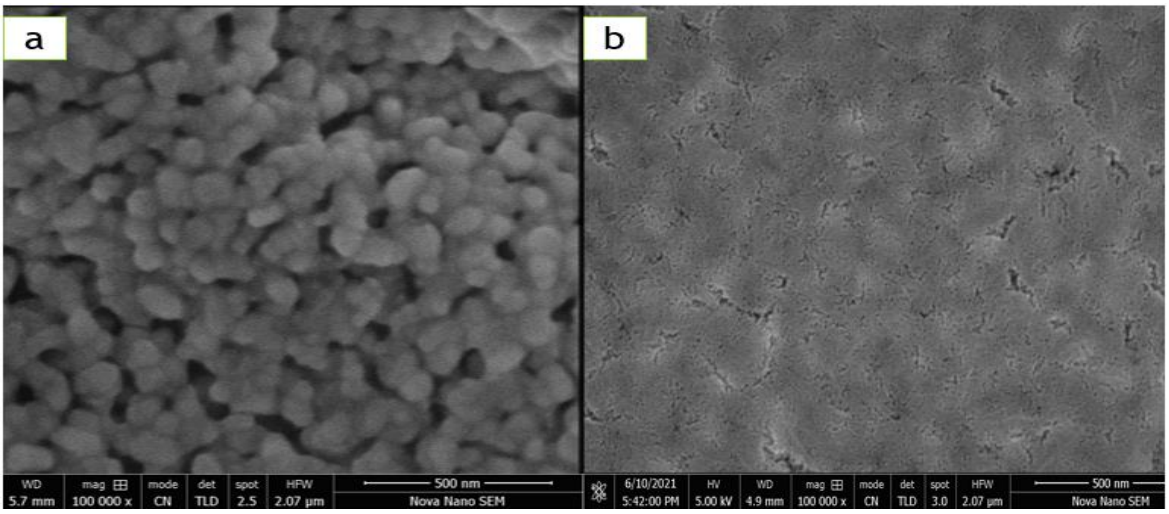


**Fig; 20 SEM images of a) $Y_2O_3$ b) NiO-$Y_2O_3$/FTO**

### 4.1.2 EDS analysis

The elemental composition and atomic distribution of the prepared thin films was confirmed by EDS technique. Figure 21 shows the EDS spectra of NiO, $ZrO_2$, $Y_2O_3$, NiO-$ZrO_2$/FTO and NiO-$Y_2O_3$ thin films which were taken after focusing different areas of the films. The analysis confirms the successful formation thin films by ensuring the presence of expected

| Element | Weight% | Atomic% |
|---|---|---|
| O K | 39.69 | 75.56 |
| Si K | 10.35 | 11.23 |
| Ni K | 1.46 | 0.76 |
| Sn L | 48.50 | 12.45 |
| Totals | 100.00 | |

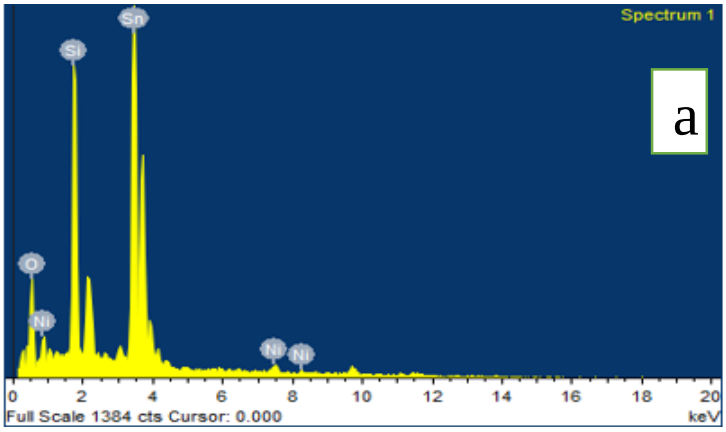


elements. Tables display the corresponding atomic and weight percentages of the elements.

| Element | Weight% | Atomic% |
|---|---|---|
| | | |
| O K | 24.09 | 69.38 |
| Si K | 1.50 | 2.46 |
| Zr L | 24.52 | 12.39 |
| Sn L | 39.98 | 15.52 |
| Pt M | 1.06 | 0.25 |
| | | |
| Totals | 91.16 | |

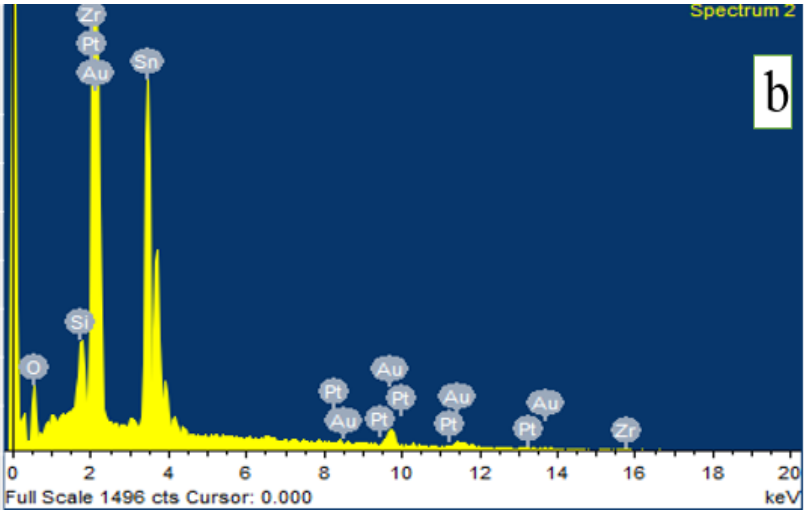


| Element | Apparent Concentration | Wt% |
|---|---|---|
| C | 1.15 | 9.32 |
| O | 30.45 | 43.22 |
| Na | 4.51 | 5.87 |
| Si | 9.52 | 13.3 |
| Ca | 1.48 | 2.11 |
| Ni | 3.49 | 5.78 |
| Zr | 10.4 | 20.41 |
| Total: | | 100 |

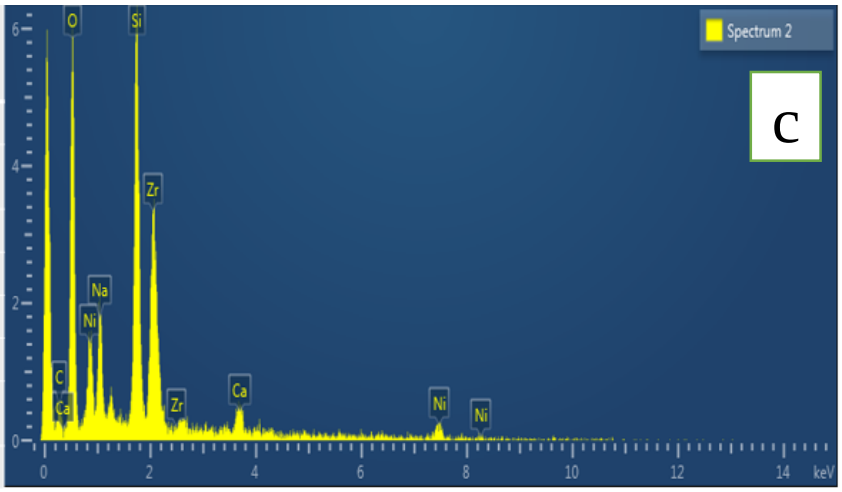


| Element | Apparent Concentration | Wt% |
|---|---|---|
| C | 0.36 | 3.79 |
| O | 9.49 | 17.25 |
| F | 15.44 | 14.88 |
| Na | 2.92 | 3.44 |
| Mg | 0.56 | 0.82 |
| Si | 9.81 | 12.72 |
| Ca | 1.6 | 2.29 |
| Y | 22.93 | 43.42 |
| Sn | 0.69 | 1.39 |
| Total: | | 100 |

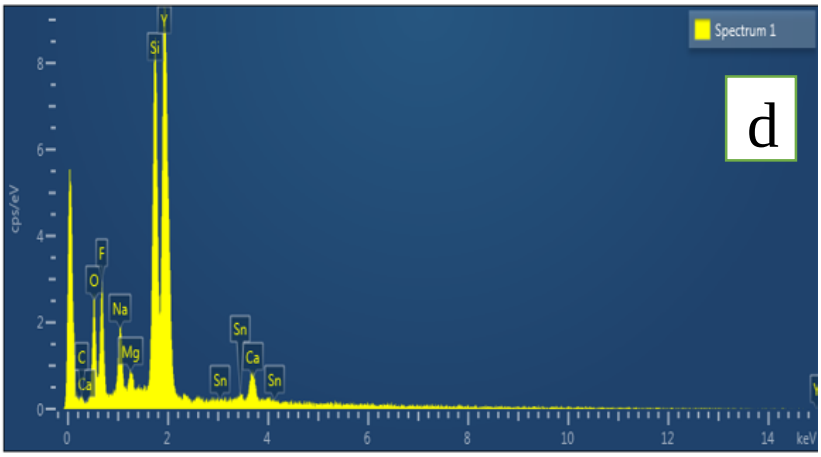

| Element | Apparent Concentration | Wt% |
|---|---|---|
| C | 0.68 | 3.79 |
| O | 14.64 | 25.69 |
| F | 2.17 | 2.53 |
| Cl | 0.41 | 0.61 |
| Ni | 12.99 | 19.28 |
| Y | 10.11 | 19.27 |
| Sn | 16.13 | 28.84 |
| Total: | | 100 |

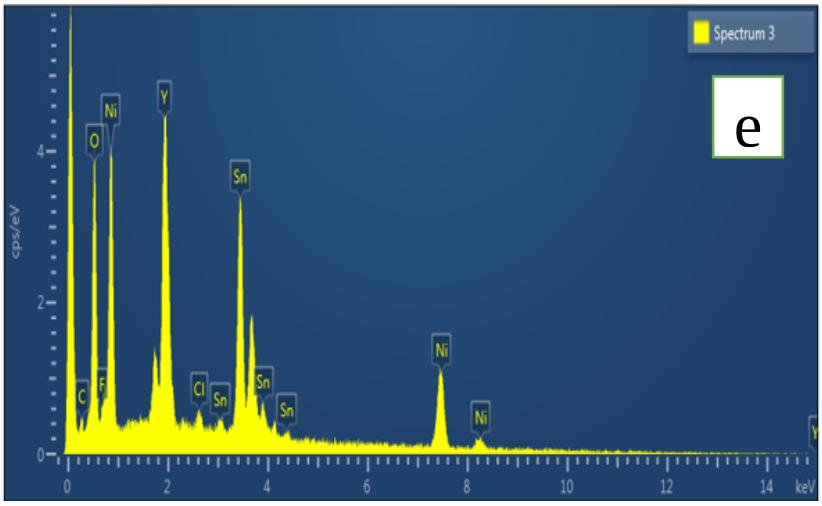


**Fig; 21 EDS spectra of a) NiO b) $ZrO_2$ c) NiO-$ZrO_2$/FTO d) $Y_2O_3$ and e) NiO-$Y_2O_3$/FTO**

### 4.1.3 XRD analysis

XRD analysis was performed to confirm the formation of mixed metal oxide composite thin film. Figure 22 shows XRD pattern of NiO, $Y_2O_3$ and NiO-$Y_2O_3$/FTO thin film. The XRD spectrum of NiO shows major diffraction peaks with 2Θ value 37.2˚, 43.3˚, 62.8˚, 75.4˚ and 79.3˚ which corresponds to (111), (200), (220), (311) and (222) reflection planes, respectively. All of these peak values perfectly coincides with the standard values of the cubic crystalline structure of NiO (JCPDS 01-073-1519) [77]. The XRD pattern of $Y_2O_3$ shows major diffraction peaks with 2Θ values 28.8˚, 33.1˚, 37.6˚ 40.45˚, 43.4˚, 47.8˚, 56.65˚, 61.8˚ and 65.8˚ which corresponds to (222), (400), (420), (332), (134), (440), (622), (543) and (642) reflection planes, respectively. The diffraction peaks of $Y_2O_3$ thin film corresponds well to the standard cubic structure (JCPDS 00-043-1036) [78]. Peaks at 26.5˚, 33.8˚, 37.9˚, 51.5˚, 61.6˚ and 65.5˚ in all the XRD patterns corresponds to FTO with tetragonal structure (JCPDS 41-1445) [79]. The XRD spectrum of NiO-$Y_2O_3$/FTO thin film shows separate diffraction peaks of both cubic NiO and cubic $Y_2O_3$ which confirms the successful formation of mixed metal oxide thin film without additional impurities.

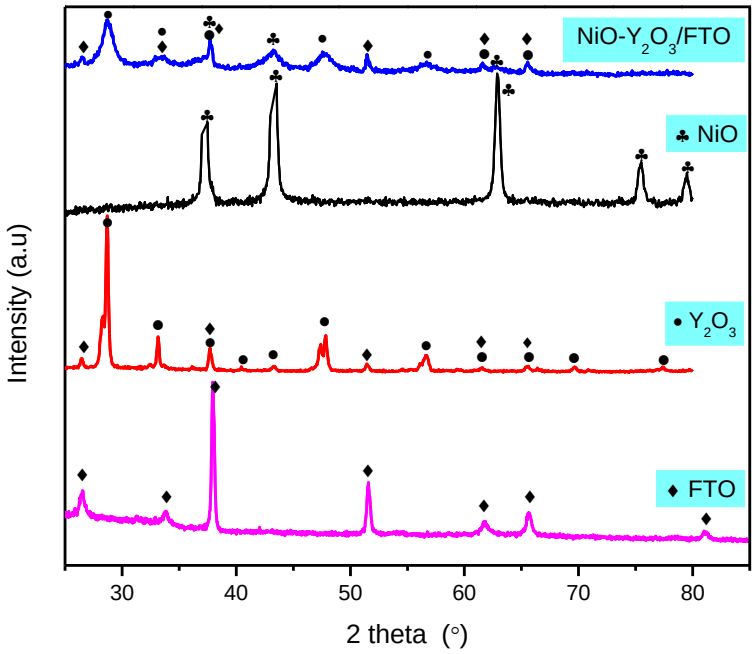


**Fig; 22. XRD pattern of NiO, $Y_2O_3$ and NiO-$Y_2O_3$/FTO thin film**

Figure 23 shows XRD pattern of pure NiO, $ZrO_2$ and NiO-$ZrO_2$/FTO thin films. The XRD spectrum of NiO shows major diffraction peaks with 2Θ value 37.2˚, 43.3˚, 62.8˚, 75.4˚ and 79.3˚ which corresponds to (111), (200), (220), (311) and (222) reflection planes respectively. All of these peak values perfectly coincides with standard values of the cubic crystalline structure of NiO (JCPDS 01-073-1519) [77]. The XRD pattern of $ZrO_2$ shows prominent diffraction peaks with 2Θ values and planes 24.0˚ (011), 28.2˚ (-111), 31.4˚ (111), 34.1˚ (200), 34.5˚ (020), 35.3˚ (002), 38.6˚ (120), 41.35˚ (-121), 44.9˚ (211), 49.3˚ (220), 50.2˚ (022), 54.1˚ (003), 55.4˚ (310), 58.0˚ (-222), 59.9˚ (131), 61.65˚ (311), 62.9˚ (113), 64.3˚ (230), 65.75˚ (023), 69.3˚ (321), 71.1˚ (-223) and 75.2˚ (140), respectively. All of the peaks are in complete accordance with monoclinic $ZrO_2$ according to JCPDS 00-037-1484. The XRD spectrum of NiO-$ZrO_2$/FTO thin film showed separate diffraction peaks of both cubic NiO and monoclinic $ZrO_2$ which confirms the successful formation of mixed metal oxide thin film without additional impurities.

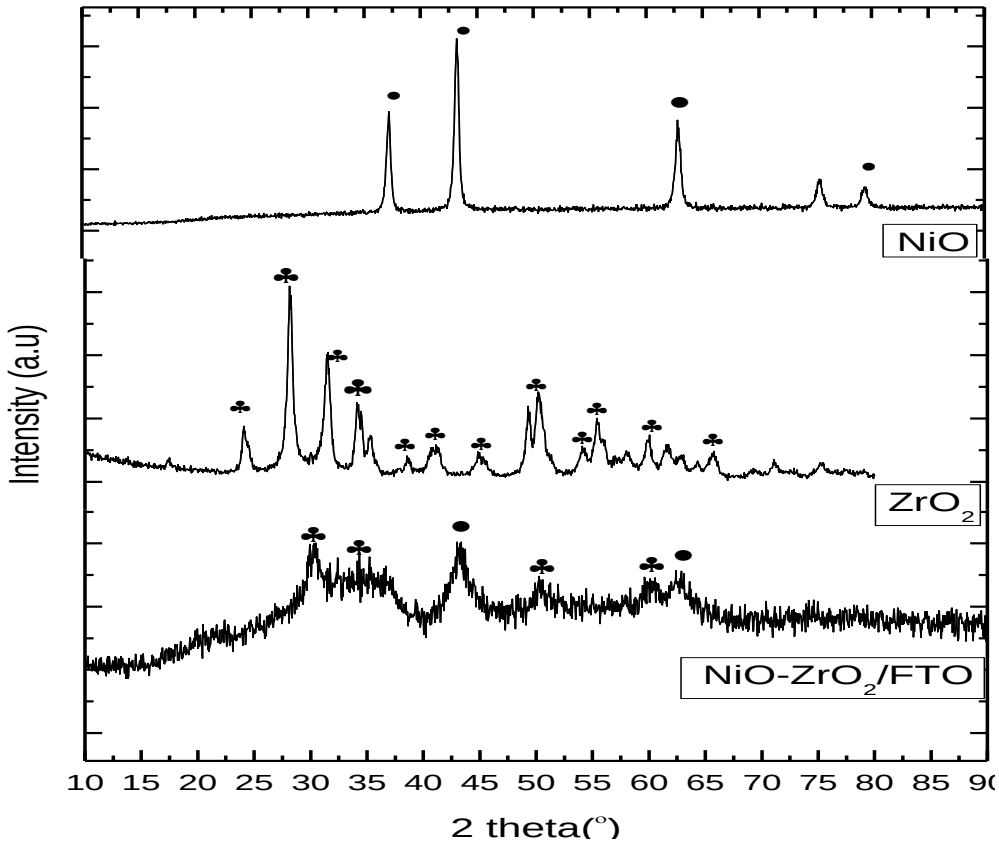


**Fig; 23 XRD pattern of pure NiO, $ZrO_2$ and NiO-$ZrO_2$/FTO thin films**

### 4.1.4 FT-IR analysis

FTIR spectra of NiO-$Y_2O_3$/FTO and NiO-$ZrO_2$/FTO thin films show no characteristic absorption bands for metal oxides because they usually appear in range below 500 $cm^{-1}$. IR absorption band at 645 $cm^{-1}$ is attributed to Sn-O bond vibration due to FTO glass substrate. The spectra reveals the formation of pure metal oxide thin films with no carbonaceous impurities present, as shown in figure 24 and 25.

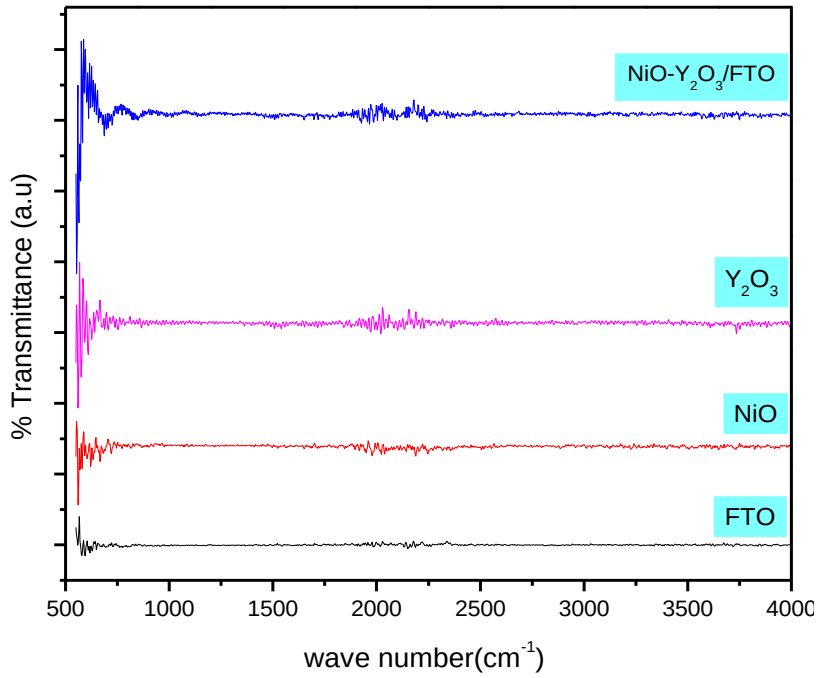


**Fig; 24. FT-IR spectra of FTO, NiO, $Y_2O_3$ and NiO-$Y_2O_3$/FTO thin films.**

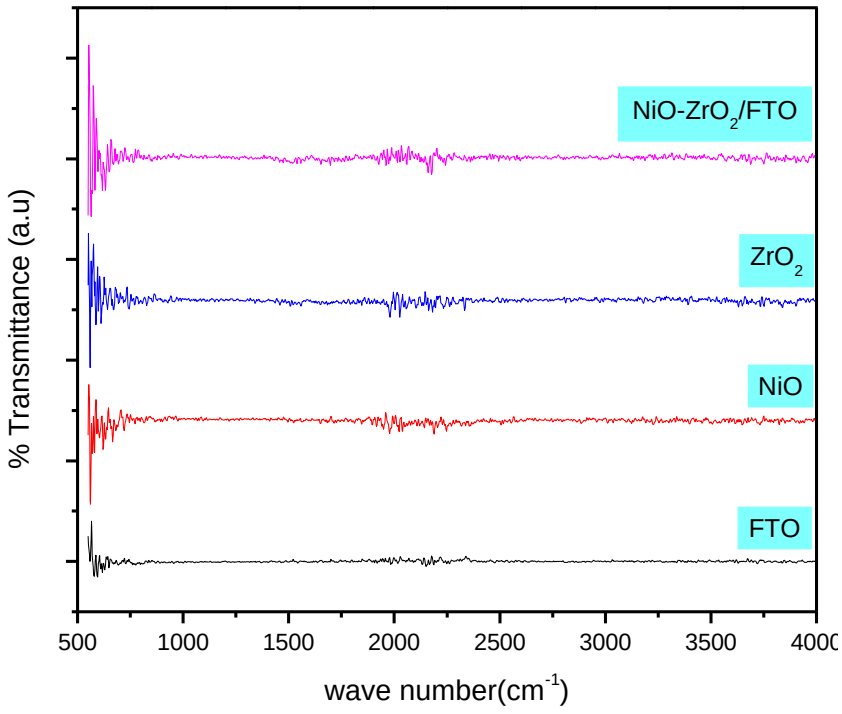


**Fig; 25. FT-IR spectra of FTO, NiO, $ZrO_2$ and NiO-$ZrO_2$/FTO thin films.**

### 4.1.5 Raman Spectroscopic analysis

Formation of mixed metal oxide thin film was further confirmed by Raman spectroscopic analysis. Fig; 26 shows Raman spectra of NiO-$Y_2O_3$/FTO thin film in comparison with pure NiO and $Y_2O_3$ thin films. NiO showed main vibrational band at 560 $cm^{-1}$ which originates from scattering of first order phonon (1P) and corresponds to LO vibrational mode. The broad band appeared at 1098 $cm^{-1}$ originates from scattering of second order phonon (2P) which corresponds to 2LO vibrational mode respectively. Pure $Y_2O_3$ thin film showed main Raman peaks at 137 $cm^{-1}$, 237 $cm^{-1}$, 297 $cm^{-1}$, 461 $cm^{-1}$ (attributed to $F_g$ vibrational mode) and at 569 $cm^{-1}$ which corresponds to $E_g$ active vibrational mode. Raman spectrum of NiO-$Y_2O_3$/FTO showed characteristic bands of both NiO and $Y_2O_3$ which confirms the formation of mixed metal oxide thin film.

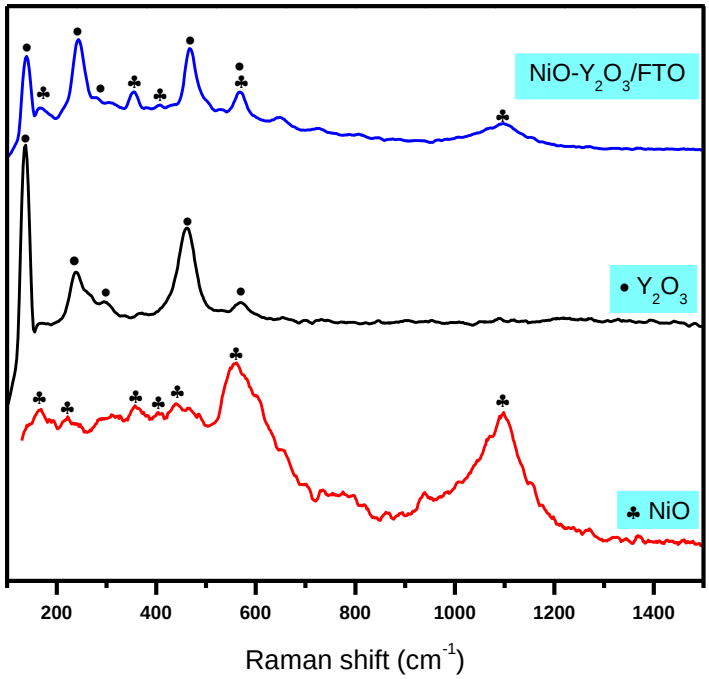


**Fig: 26. Raman spectra of NiO, $Y_2O_3$ and NiO-$Y_2O_3$/FTO thin film.**

Fig; 27shows Raman spectra of NiO-$ZrO_2$/FTO thin film in comparison with pure NiO and $ZrO_2$ thin films. Pure $ZrO_2$ showed main peaks at 173 $cm^{-1}$ (Bg), 324$cm^{-1}$($B_{1g}$), 462 $cm^{-1}$($E_g$) and 603 $cm^{-1}$($B_{1g}$). Raman spectrum of NiO-$ZrO_2$/FTO showed characteristic bands of both NiO and $ZrO_2$ which confirms the formation of mixed metal oxide thin film.

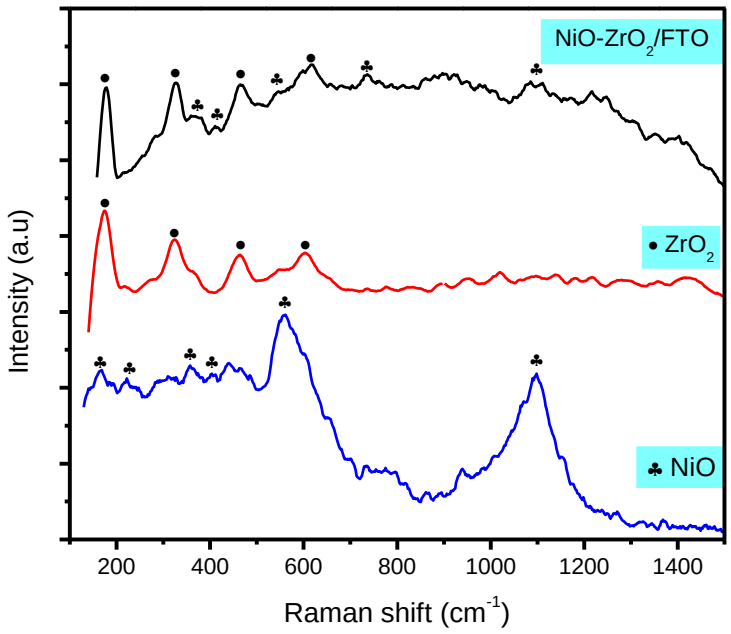


**Fig: 27. Raman spectra of NiO, $ZrO_2$ and NiO-$ZrO_2$/FTO thin film.**

### 4.2 Electrochemical oxidation of methanol via prepared metal oxide thin films

#### 4.2.1 Cyclic Voltammetry (CV)

##### 4.2.1.1 Electrocatalytic performance of NiO-$Y_2O_3$/FTO thin films

Electrocatalytic performance of prepared metal oxide thin films towards methanol oxidation was carried out in 0.5M NaOH electrolyte solution at a scan rate of 100 mV/s using Pt wire as counter electrode, Ag/AgCl as reference electrode and prepared metal oxide composite thin film as working electrode. Figure 28 represents cyclic voltammogram of synthesized NiO-$Y_2O_3$/FTO thin film recorded before and after addition of 0.8M methanol solution to the reaction medium. It can be seen that in the absence of methanol no prominent oxidation peaks are observed, only a small reduction peak at 0.34V in the backward scan is observed which is attributed to $Ni(OH)_2$/NiOOH reduction reaction[80]. A prominent methanol oxidation peak at 0.65V with current density value of 7 $mA/cm^2$ is observed in cathodic half cycle with 0.8 M methanol solution at scan rate of 100mV/s. Appearance of oxidation peak in reverse scan reveals that methanol oxidation continues in cathodic half cycle as well. This behaviour can be explained as, oxidation peak obtained in anodic scan is due to oxidation of freshly chemosorbed methanol to carbonaceous intermediate species parallel to oxidation of $Ni^{+2}$ and $Ni^{+3}$ species[80]. Oxidation of $Ni^{+2}$ and $Ni^{+3}$ species along with deposition of carbonaceous intermediates/products on working electrode (electrode poising) results in decreasing the availability of active sites for overall methanol oxidation. Thus, when potential was swept

cathodically methanol oxidation continues and a maximum oxidation peak current is obtained associated with oxidation of carbonaceous species not completely oxidized in the anodic scan and availability of active sites for adsorption of methanol.

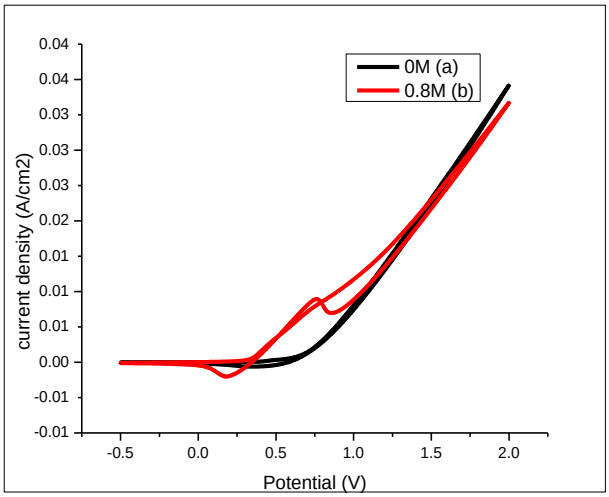


**Fig; 28 Cyclic voltammogram of NiO-$Y_2O_3$/FTO thin films in 0.5M NaOH solution at 100 mV/s. a) In absence of methanol b) 0.8 M methanol solution.**

For comparative studies, cyclic voltammograms obtained with NiO-$Y_2O_3$ thin films were compared with pure NiO and $Y_2O_3$ as shown in the figure 29. No prominent oxidation peaks were observed with pure NiO and $Y_2O_3$ in 0.8M methanol solution and 0.5M NaOH at scan rate of 100mV/s which is attributed to the synergistic effect between metal oxides in mixed metal oxide thin films.

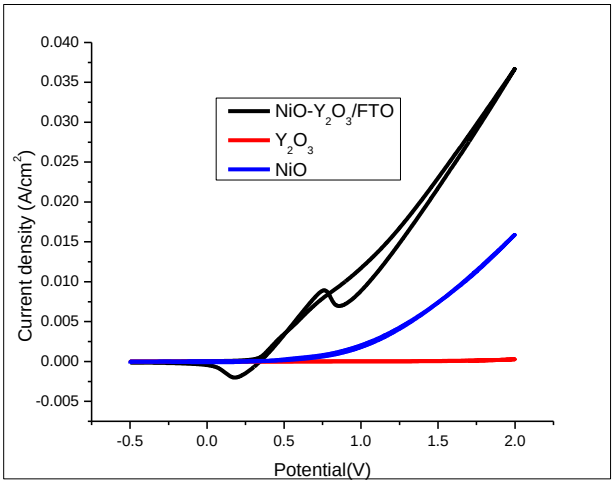


**Fig; 29 Cyclic voltammogram of NiO, $Y_2O_3$ and NiO-$Y_2O_3$/FTO thin films in 0.5M NaOH and 0.8M methanol solution at 100 mV/s.**

### 4.2.1.2 Effect of methanol concentration on electrocatalytic performance of NiO-$Y_2O_3$/FTO thin films

Dependence of electrocatalytic behaviour of synthesized metal oxide thin films on methanol concentration was also studied. Figure 30 represents cyclic voltammogram of NiO-$Y_2O_3$/FTO thin films, recorded in 0.5M NaOH electrolyte solution at a scan rate of 100 mV/s using Pt wire as counter electrode, Ag/AgCl as reference electrode and prepared metal oxide composite thin film as working electrode, before and after addition of (0.2, 0.4, 0.6, 0.8, and 1M) methanol solution to the reaction medium. It can be seen that peak current density for methanol oxidation steadily increases as methanol concentration increases, which means current density of oxidation peaks depends on bulk concentration of methanol and oxidation of methanol is diffusion controlled process. Additionally, methanol oxidation peaks shifted towards higher potential with increasing methanol concentration which might be attributed to increased concentration of unoxidized carbonaceous products which need higher potential to be oxidized plus saturation of active sites which leads to slowing down the oxidation process. Table 1 represents peak current densities for different concentrations of methanol at specified potentials.

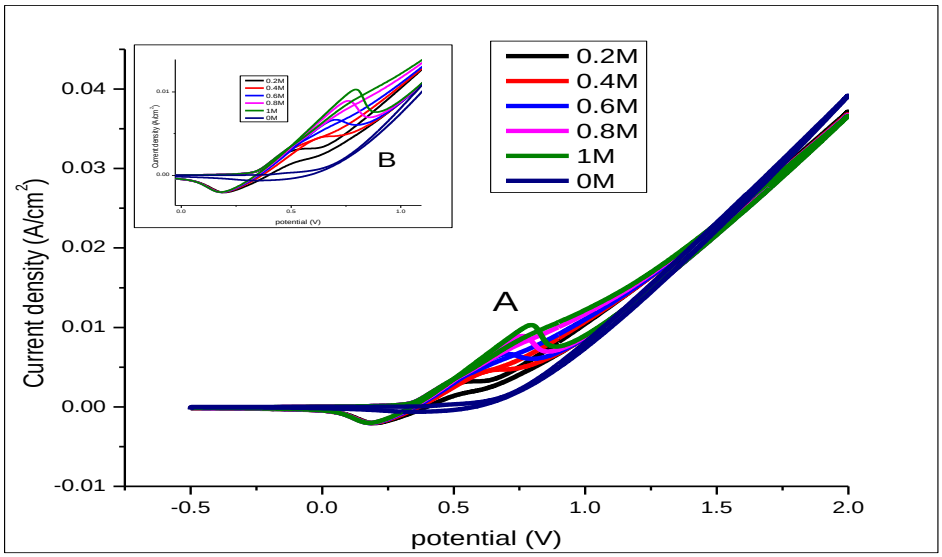


**Fig; 30. Cyclic voltammogram of NiO-$Y_2O_3$/FTO thin films in 0.5M NaOH solution at 100mV/s. A) In the presence of 0, 0.2, 0.4, 0.6, 0.8 and 1M methanol solution B) zoomed panel of oxidation peaks.**

**Table; 1. Peak current densities for different concentrations of methanol at specified potentials.**

| S.No | Methanol concentration | Current density at 0.65V ($mA/cm^2$) | Onset Potential (V) |
|---|---|---|---|
| 1 | 0.2 M | 3.5 | 0.33 |
| 2 | 0.4 M | 4.8 | 0.33 |
| 3 | 0.6 M | 6.2 | 0.33 |
| 4 | 0.8 M | 7.0 | 0.33 |
| 5 | 1 M | 7.3 | 0.33 |

### 4.2.1.3 Effect of scan rate on electrocatalytic performance of NiO-$Y_2O_3$/FTO thin films

The effect of different scan rates on electrocatalytic performance of NiO-$Y_2O_3$/FTO thin films was studied in 0.5M NaOH electrolyte solution against Ag/AgCl reference electrode and Pt as counter electrode in the presence of 0.6M methanol solution. Cyclic voltammograms in figure 31 shows that peak current density increases with increase in the scan rate (from 25mV/s to 150mV/s), which underpins the fact that oxidation of methanol is diffusion-controlled process. Increase in scan rate increases electron transfer process which ultimately enhances the peak current density. Additionally, as can be seen in the figure the oxidation peak slightly shifts towards positive potential with increase in the scan rate which is attributed to the IR drop generated at high current density.

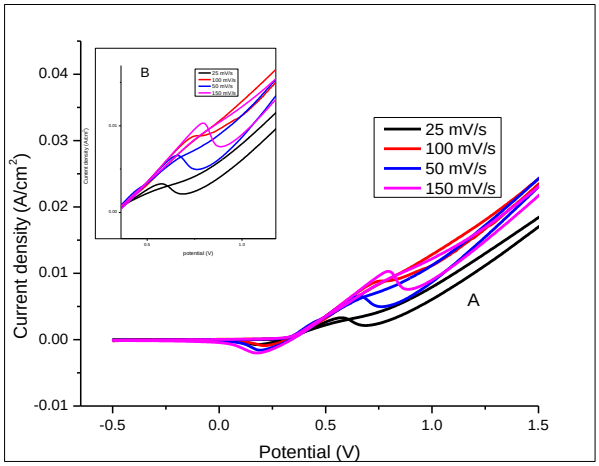


**Fig; 31 Cyclic voltammogram of NiO-$Y_2O_3$/FTO thin films in 0.5M NaOH and 0.6M methanol solution at scan rates of A) 25, 50, 100 and 150mV/s B) zoomed panel of oxidation peaks.**

#### 4.2.1.4 Effect of concentration of Ni:Y precursor solution on the electrocatalytic performance of NiO-$Y_2O_3$/FTO thin films

To analyse the effect of concentration of NiO and $Y_2O_3$ on the electrocatalytic performance of NiO-$Y_2O_3$/FTO, thin films were deposited from precursor solutions with different Ni:Y concentrations (0.09:0.01, 0.01:0.09, 0.07:0.03, 0.03;0.07). Cyclic voltammograms of these thin films recorded with 0.5M NaOH and 0.8M methanol at scan rate of 100mv/s were compared with thin film of NiO:$Y_2O_3$ (0.1:0.1) as shown in the figure 32. Thin film with 0.1: 0.1 precursor concentration showed best results with oxidation peak at the lowest potential of 0.7V and lowest onset potential as represented by table 2.

**Table; 2 Current density values of thin films with different Ni:Y concentration at specified potential.**

| Ni: Y | Current Density at 0.65V ($mA/cm^2$) | Onset Potential (V) |
|---|---|---|
| 0.09: 0.01 | 4.9 | 0.39 |
| 0.01: 0.09 | 4.4 | 0.41 |
| 0.07: 0.03 | 4.0 | 0.37 |
| 0.03: 0.07 | 5.6 | 0.39 |
| 0.1: 0.1 | 6.2 | 0.31 |

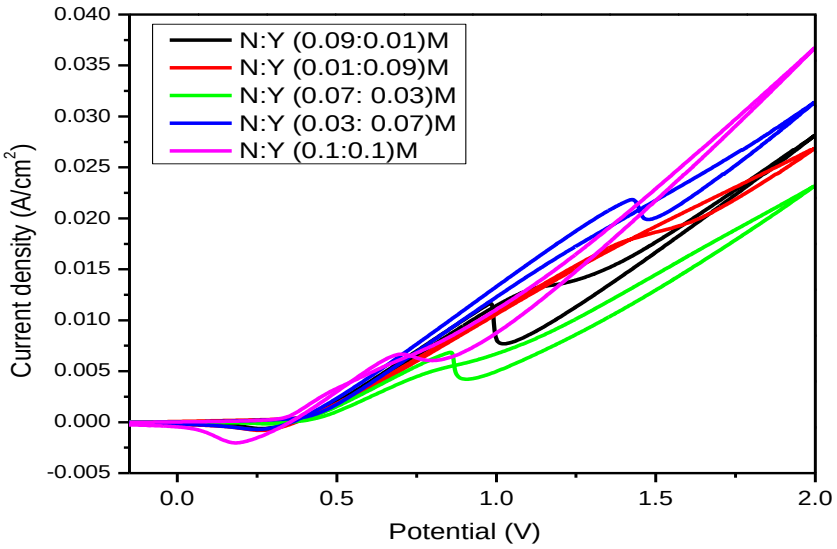


**Fig: 32. Cyclic voltammogram of NiO-$Y_2O_3$/FTO thin films deposited from different precursor solutions with different Ni:Y concentration**.

### 4.2.2.1 Electrocatalytic performance of (NiO-$ZrO_2$/FTO) thin films

Electrocatalytic performance of prepared NiO-$ZrO_2$/FTO metal oxide thin films towards methanol oxidation was also carried out in 0.5M NaOH electrolyte solution at a scan rate of 100 mV/s using Pt wire as counter electrode, Ag/AgCl as reference electrode and prepared metal oxide composite thin film as working electrode. Figure 33 represents cyclic voltammogram of synthesized NiO-$Zr_2O_3$/FTO thin films recorded before and after addition of 0.6M methanol solution to the reaction medium. It can be seen that in the absence of methanol no prominent oxidation peaks are observed, only a small reduction peak at 0.28V in the backward scan is observed which is attributed to $Ni(OH)_2$/NiOOH reduction reaction[80]. A prominent methanol oxidation peak at 0.65 V with current density value of 10 mA/cm$^2$ is observed in anodic half cycle with 0.6 M methanol solution at scan rate of 100mV/s. Appearance of oxidation peak in reverse scan reveals that methanol oxidation continues in cathodic half cycle as well. This behaviour can be explained as, oxidation peak obtained in anodic scan is due to oxidation of freshly chemosorbed methanol to carbonaceous intermediate species parallel to oxidation of $Ni^{+2}$ and $Ni^{+3}$ species[80]. Oxidation of $Ni^{+2}$ and $Ni^{+3}$ species along with deposition of carbonaceous intermediates/products on working electrode (electrode poising) results in decreasing the availability of active sites for overall methanol oxidation. Thus, when potential was swept cathodically methanol oxidation continues and a maximum oxidation peak current is obtained associated with oxidation of

carbonaceous species not completely oxidized in the anodic scan and availability of active sites for adsorption of methanol.

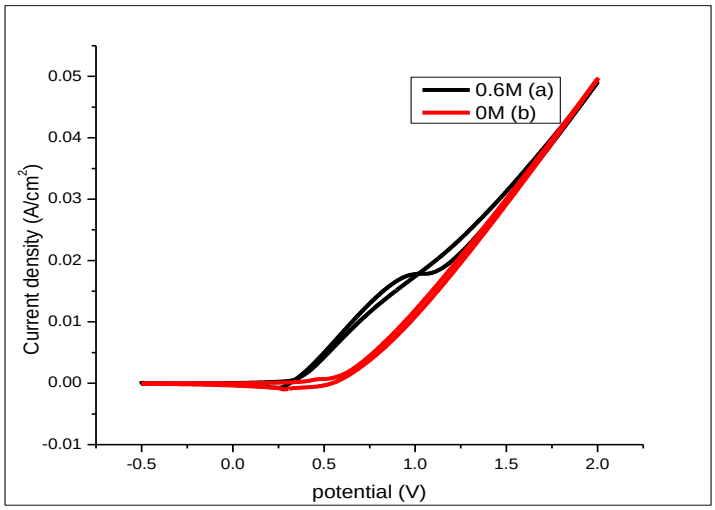


**Fig; 33. Cyclic voltammogram of NiO-$ZrO_2$/FTO thin films in 0.5M NaOH solution at 100 mV/s. a) In absence of methanol b) 0.6 M methanol solution.**

For comparative studies, cyclic voltammograms obtained with NiO-$ZrO_2$ thin films were compared with pure NiO and $ZrO_2$ as shown in the figure 34. No prominent oxidation peaks were observed with pure NiO and $ZrO_2$ in 0.6M methanol solution and 0.5M NaOH at scan rate of 100mV/s which is attributed to the synergistic effect between metal oxides in mixed metal oxide thin films.

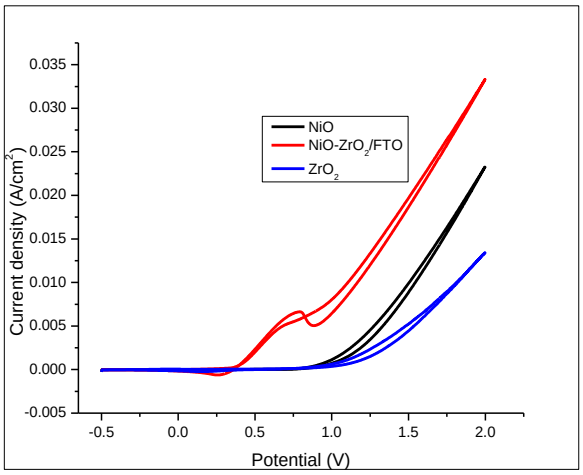


**Fig; 34. Cyclic voltammogram of NiO, $ZrO_2$ and NiO-$ZrO_2$/FTO thin films in 0.5M NaOH and 0.6M methanol solution at 100 mV/s.**

### 4.2.2.2 Effect of methanol concentration on electrocatalytic performance of NiO-$ZrO_2$/FTO thin films

Dependence of electrocatalytic behaviour of synthesized metal oxide thin films on methanol concentration was also studied. Figure 35 represents cyclic voltammogram of NiO-$ZrO_2$/FTO thin films, recorded in 0.5M NaOH electrolyte solution at a scan rate of 100 mV/s using Pt wire as counter electrode, Ag/AgCl as reference electrode and prepared metal oxide composite thin film as working electrode, before and after addition of (0.2, 0.4, 0.6, 0.8, and 1M) methanol solution to the reaction medium. It can be seen that peak current density for methanol oxidation steadily increases as methanol concentration increases, which means current density of oxidation peaks depends on bulk concentration of methanol and oxidation of methanol is diffusion controlled process. Additionally, methanol oxidation peaks shifted towards higher potential with increasing methanol concentration which might be attributed to increased concentration of unoxidized carbonaceous products which need higher potential to be oxidized plus saturation of active sites which leads to slowing down the oxidation process. Table 3 represents peak current densities for different concentrations of methanol at specified potentials.

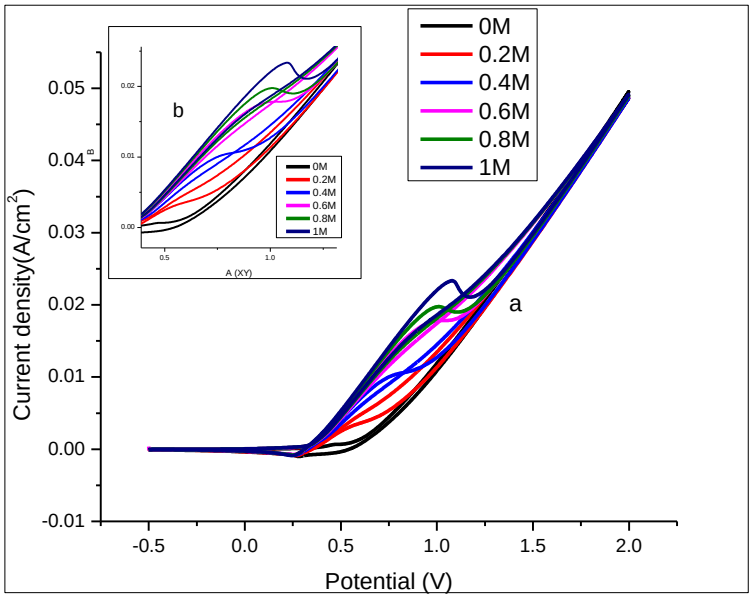


**Fig; 35 Cyclic voltammogram of NiO-$ZrO_2$/FTO thin films in 0.5M NaOH solution at 100mV/s. A) In the presence of 0, 0.2, 0.4, 0.6, 0.8 and 1M methanol solution B) zoomed panel of oxidation peaks.**

**Table; 3 Peak current densities for different concentrations of methanol at specified potentials.**

| S.No | Methanol concentration | Current density at 0.65 ($mA/cm^2$) | Onset Potential (V) |
|---|---|---|---|
| 1 | 0.2M | 5.5 | 0.35 |
| 2 | 0.4M | 8.1 | 0.35 |
| 3 | 0.6M | 9.9 | 0.33 |
| 4 | 0.8M | 10.4 | 0.33 |
| 5 | 1M | 10.8 | 0.33 |

### 4.2.2.3 Effect of scan rate on electrocatalytic performance of NiO-$ZrO_2$/FTO thin films

The effect of different scan rates on electrocatalytic performance of NiO-$ZrO_2$/FTO thin films was studied in 0.5M NaOH electrolyte solution against Ag/AgCl reference electrode and Pt as counter electrode in the presence of 0.6M methanol solution. Cyclic voltammograms in figure 36 shows that peak current density increases with increase in the scan rate (from 25mV/s to 150mV/s), which underpins the fact that oxidation of methanol is diffusion-controlled process. Increase in scan rate increases electron transfer process which ultimately enhances the peak current density. Additionally, as can be seen in the figure the oxidation peak slightly shifts towards positive potential with increase in the scan rate which is attributed to the IR drop generated at high current density.

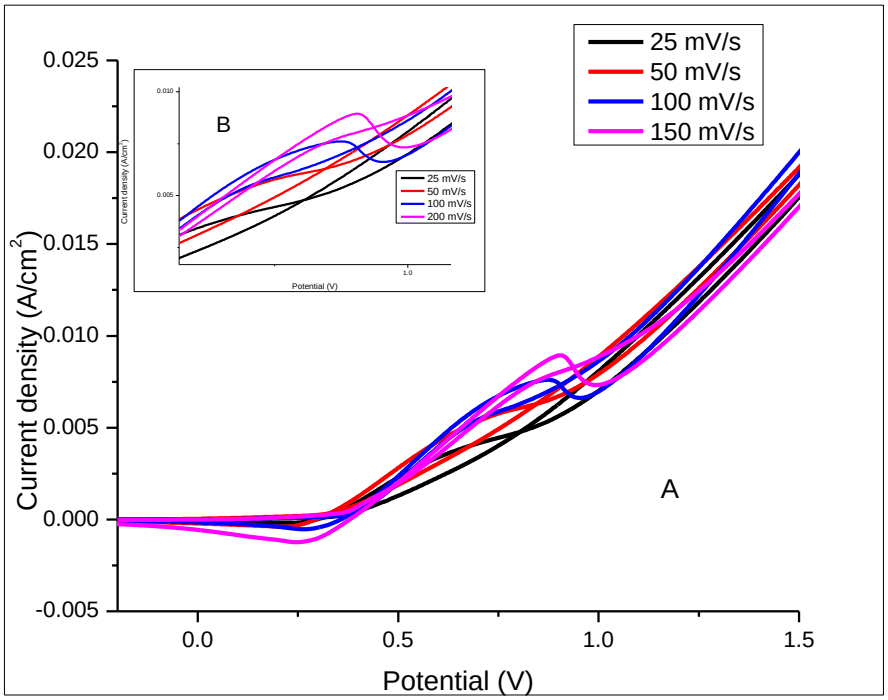


**Fig; 36 Cyclic voltammogram of NiO-$ZrO_2$/FTO thin films in 0.5M NaOH and 0.6M methanol solution at scan rates of A) 25, 50, 100 and 150mV/s B) zoomed panel of oxidation peaks.**

### 4.2.2.4 Effect of concentration of Ni:Zr precursor on the electrocatalytic performance of NiO-$ZrO_2$/FTO thin films

To study the effect of concentration of NiO and $ZrO_2$ on the electrocatalytic performance of NiO-$ZrO_2$/FTO, thin films were deposited from precursor solutions with different Ni:Zr concentrations (0.09:0.01, 0.01:0.09, 0.07:0.03, 0.03;0.07). Cyclic voltammograms of these thin films recorded in 0.5M NaOH electrolyte and 0.8M methanol at scan rate of 100mv/s were compared with thin film of NiO:$ZrO_2$ (0.1:0.1) as shown in the figure 37. Thin film with 0.1: 0.1 precursor concentration showed best results with oxidation peak at the lowest potential of 0.9V and lowest onset potential as represented by the table 4.

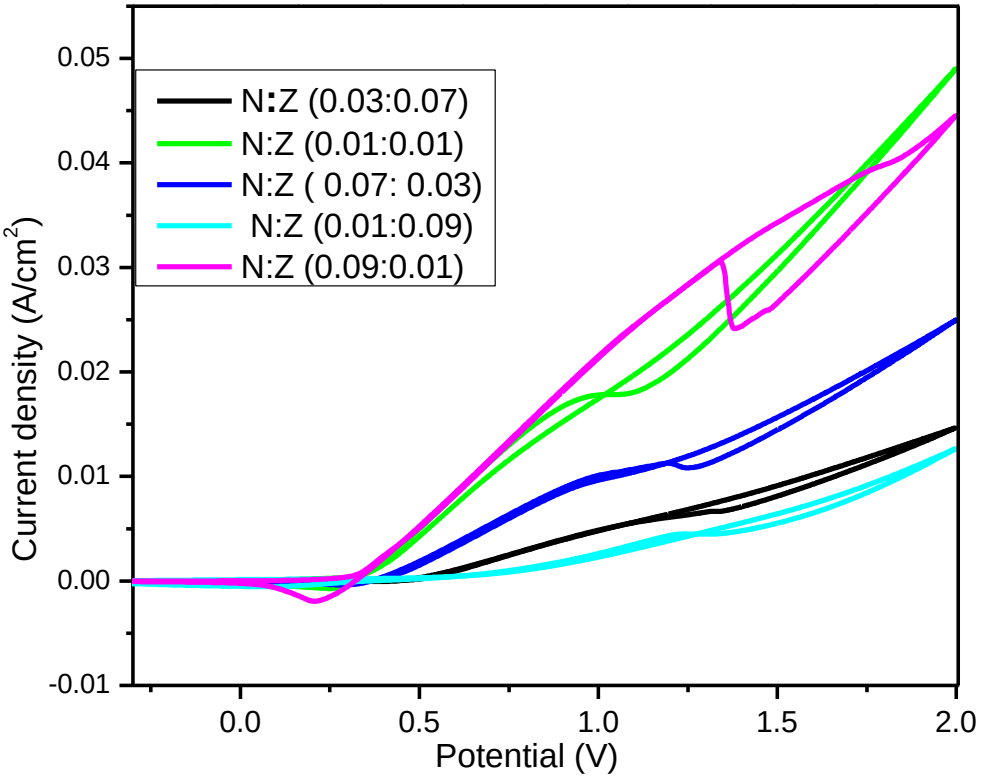


**Fig: 37 cyclic voltammogram of NiO-$ZrO_2$/FTO thin films deposited from different from precursor solutions with different NiO:$ZrO_2$ concentration.**

**Table; 4 Current density values of thin films with different Ni:Zr precursor concentration at specified potential.**

| **NiO: $ZrO_2$** | **Current Density at 0.65 (mA/cm$^2$)** | **Onset Potential (V)** |
|---|---|---|
| 0.09: 0.01 | 9.8 | 0.33 |
| 0.07: 0.03 | 4.8 | 0.39 |
| 0.03: 0.07 | 1.5 | 0.56 |
| 0.1: 0.1 | 10.1 | 0.31 |

### 4.2.2 Chronoamperometry

The electrocatalytic oxidation of methanol by prepared films was further studied via chronoamperometry. The analysis was carried out in the presence of 0.5M NaOH electrolyte solution, Ag/AgCl as reference, Pt as counter and prepared film as working electrode. Chronoamperogram was recorded for time period of 2000 seconds with addition of 0.2M methanol after every 90 seconds at applied potential of 0.6V. Current-time plot of NiO-$ZrO_2$/FTO thin film shows increase in current on addition of methanol with time as depicted in figure 38. This implies efficient electrocatalytic activity of prepared thin film towards methanol oxidation. Chronoamperogram for NiO-$Y_2O_3$/FTO thin film was also recorded under same experimental parameters. Current-time plot shown in figure 39 demonstrates increase in current on methanol addition through whole operating time period of 2000 seconds. Chronoamperogram shown in figure 40 and 41were recorded in the presence of 0.6 M methanol for time period of 2000 seconds to check the stability of prepared thin films towards methanol oxidation. NiO-$ZrO_2$/FTO and NiO-$Y_2O_3$/FTO thin films observed current decay of 10% and 6.8% of initial current density values. This decay may be due to the reduction of methanol concentration near electrode surface with time or due to accumulation of carbonaceous reaction intermediates like CO on electrode surface.

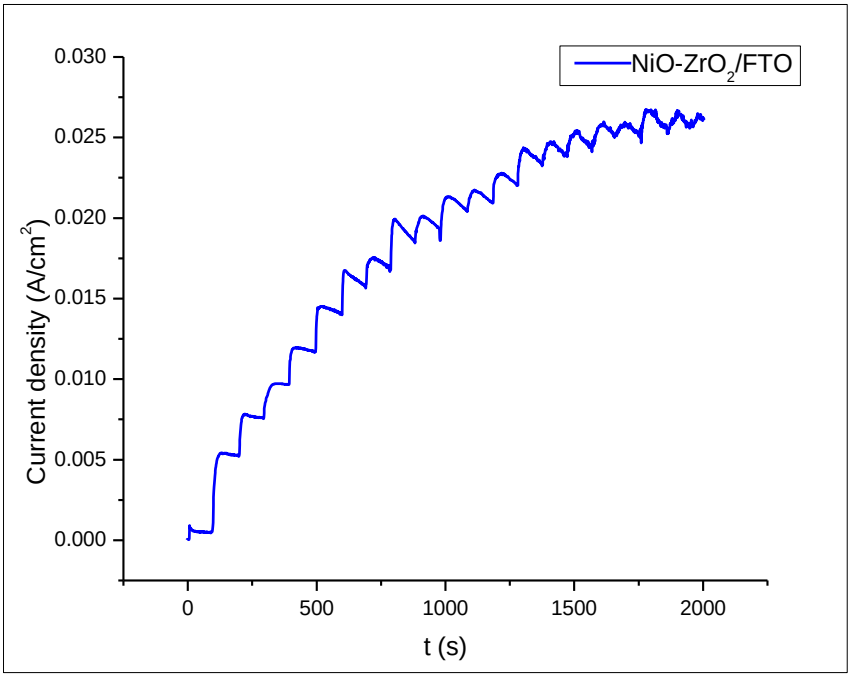


**Fig; 38. Curent-time plot of NiO-$ZrO_2$/FTO thin film in 0.5M NaOH electrolyte solution at applied potential of 0.6V.**

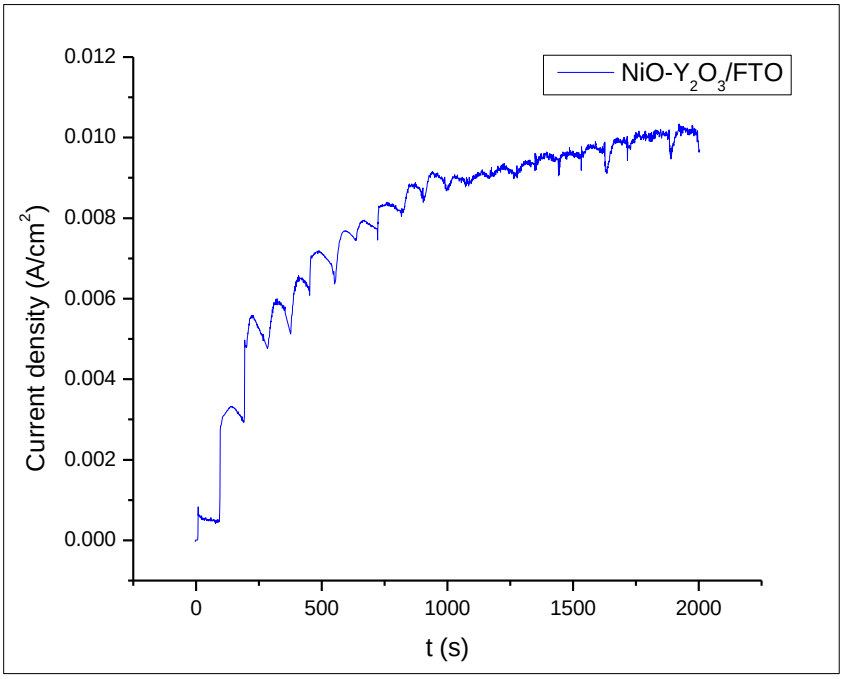


**Fig; 39. Curent-time plot of NiO-$Y_2O_3$/FTO thin film in 0.5M NaOH electrolyte solution at applied potential of 0.6V.**

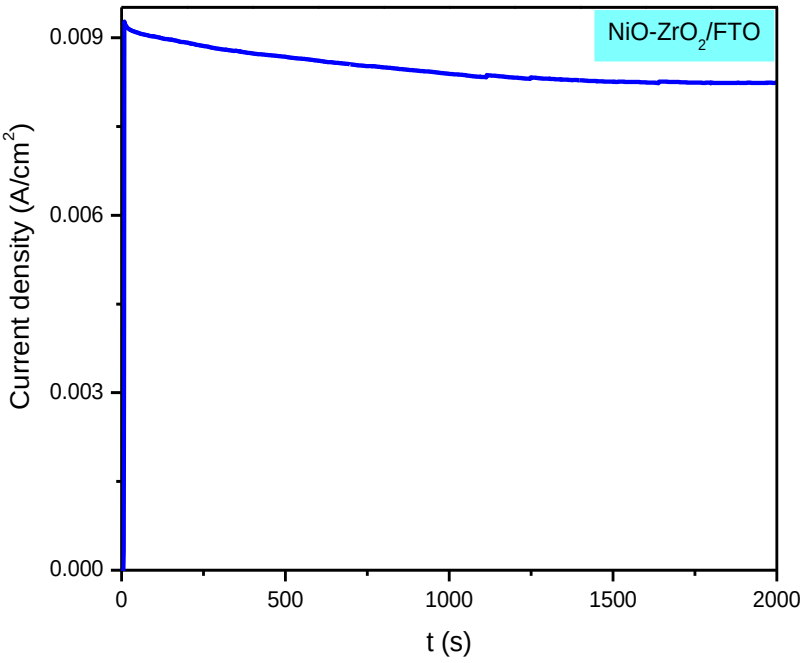


**Fig; 40. Curent-time plot of NiO-$ZrO_2$/FTO thin film in 0.5M NaOH and 0.6 M methanol solution at applied potential of 0.6V.**

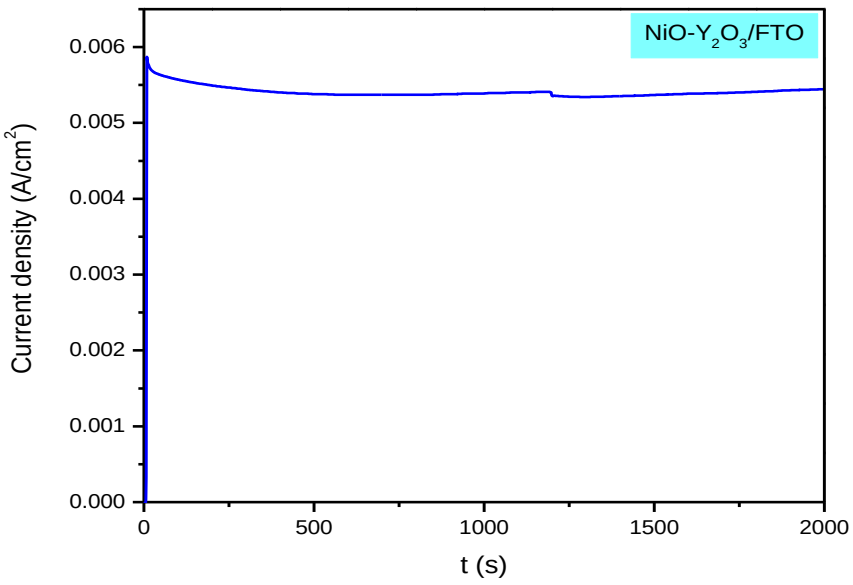


**Fig; 41 Curent-time plot of NiO-$Y_2O_3$/FTO thin film in 0.5 M NaOH and 0.6 M methanol solution at applied potential of 0.6V.**

### 4.2.3 Electrochemical impedance study

Electrochemical impedance studies were conducted to evaluate the charge transfer dynamics on the prepared metal oxide thin films surfaces. For both films analysis was carried out in the presence of 0.6M methanol and 0.5M NaOH electrolyte solution at DC voltage of 0.6V while using Ag/AgCl as reference and Pt as counter electrode. Figure 42 represents Nyquist plot of NiO-$ZrO_2$/FTO thin film in comparison to pure NiO and $ZrO_2$. As can be seen mixed metal oxide thin films exhibits the smallest semicircle with $R_{ct}$ value of 34.14Ω compared to pure NiO and $ZrO_2$ with $R_{ct}$ values of 88.42Ω and 2779Ω respectively. This decrease in charge transfer resistance of mixed metal oxide thin film is associated with enhanced electron transfer process due to synergistic effect and efficient oxidation of methanol. Figure 43 represents Nyquist plot of NiO-$ZrO_2$/FTO thin film in the presence and absence of methanol. A semicircle with smaller diameter and $R_{ct}$ value of 34.14Ω is observed in the presence of 0.6M methanol compared to larger semicircle with $R_{ct}$ value 59.74Ω recorded in the absence of methanol. These results can be explained on the basis of the fact that presence of methanol enhances reaction kinetics.

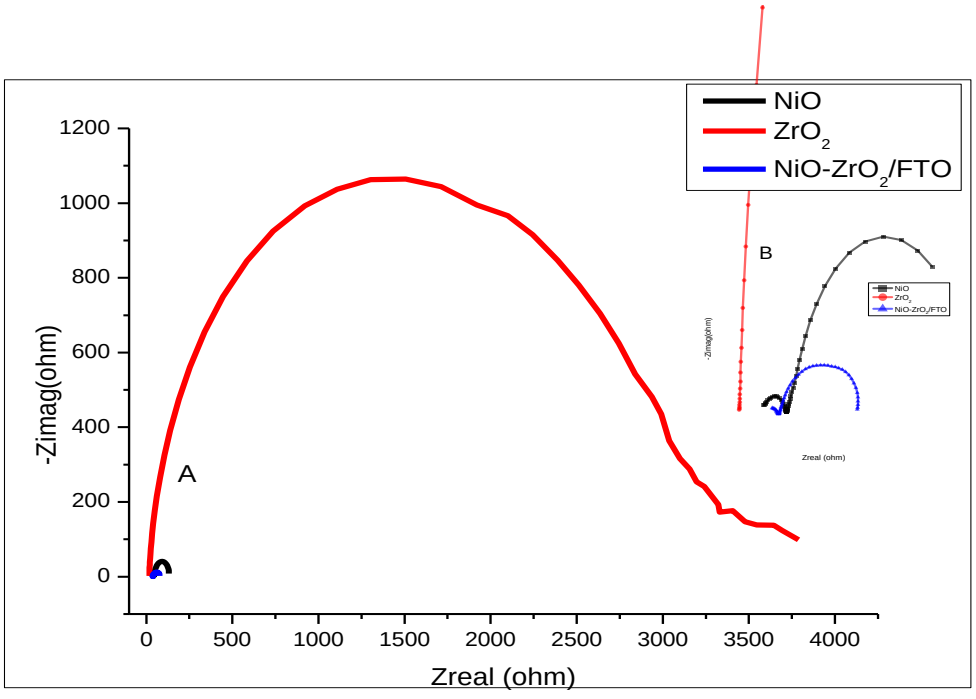


**Fig: 42. A) Nyquist plot of NiO, $ZrO_2$ and NiO-$ZrO_2$/FTO thin film in 0.5M NaOH/0.6M MeOH at 0.6V. B) Zoomed panel of semicircles**

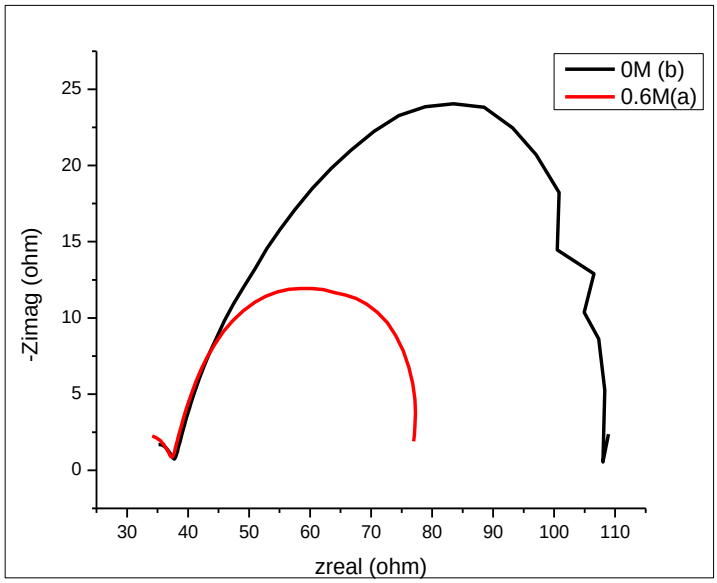


**Fig; 43. Nyquist plot of NiO-$ZrO_2$/FTO thin film a) in the presence of 0.6M methanol b) in the absence of methanol.**

Electrochemical impedance study of NiO-$Y_2O_3$/FTO thin film was also was carri ed out in the presence of 0.6M methanol and 0.5M NaOH electrolyte solution at DC voltage of 0.6V while using Ag/AgCl as reference and Pt as counter electrode. Figure 44 represents Nyquist plot of NiO-$Y_2O_3$/FTO thin film in comparison to pure NiO and $Y_2O_3$ thin films. As can be seen, mixed metal oxide thin films exhibits the smallest semicircle with $R_{ct}$ value of 22.8Ω compared to pure NiO and $Y_2O_3$ with $R_{ct}$ values of 88.4Ω and 3189Ω respectively. This decrease in charge transfer resistance of mixed metal oxide thin film is associated with enhanced electron transfer process due to synergistic effect plus availability of large surface area as a result of combination of mixed metal oxides. Figure 45 represents Nyquist plot of NiO-$Y_2O_3$/FTO thin film in the presence and absence of methanol. A semicircle with smaller diameter and $R_{ct}$ value of 22.8Ω is observed in the presence of 0.6M methanol compared to larger semicircle with $R_{ct}$ value of 66.64Ω recorded in the absence of methanol.

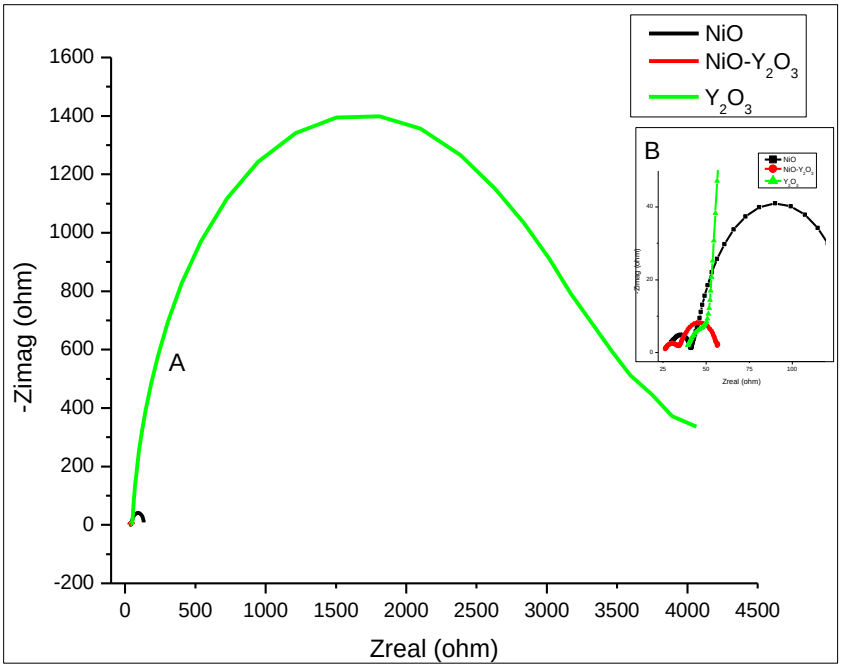


**Fig: 44. A) Nyquist plot of NiO, $Y_2O_3$ and NiO-$Y_2O_3$/FTO thin film in 0.5M NaOH/0.6M MeOH at 0.6V B) Zoomed panel of semicircles.**

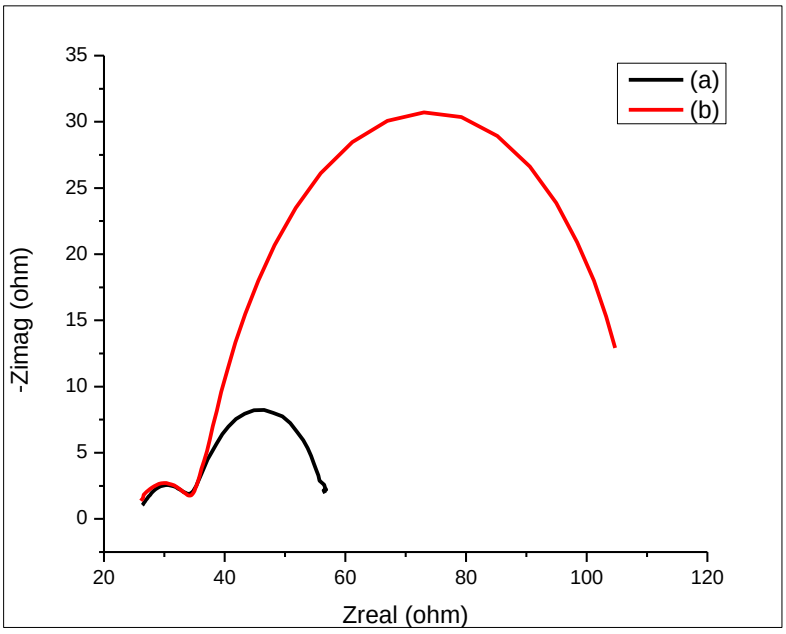


**Fig; 45 Nyquist plot of NiO-$Y_2O_3$/FTO thin film a) in the presence of 0.6M methanol b) in the absence of methanol.**

## Conclusions

From the last decade fuel cells are popular as best alternative to meet power generation demands. DMFCs encounter challenges which make their commercialization unfavourable, like high manufacturing costs mainly due to expansive catalysts being used. The present work focused on the fabrication of cost friendly electro-catalysts for the oxidation of methanol with enhanced efficiency. NiO, $ZrO_2$, $Y_2O_3$, NiO-$ZrO_2$/FTO and NiO-$Y_2O_3$/FTO thin films were deposited on FTO glass substrate via simple dip coating method. The precursors used were $Ni(OAc)_2.2H_2O$, $Zr(CH_3COO)_4$, $Y(CH_3COO)_3.H_2O$ salts which were easily soluble in organic solvents. Different characterization techniques were used to characterize the prepared thin films. SEM confirmed the uniformity and porosity while EDS confirmed the elemental composition of the prepared thin films. Other techniques like XRD, Raman spectroscopy and FT-IR revealed the crystallinity phases and successful formation of mixed metal oxide thin films without any additional impurities.

Electrocatalytic behaviour of prepared thin films towards methanol oxidation was studied using potentiostat based on three electrode system, in 0.5M NaOH electrolyte solution at scan rate of 100 mV/s, using Pt wire as counter electrode, Ag/AgCl as reference electrode and prepared metal oxide composite thin film as working electrode, providing potential range of -0.5 to 2.0V. Different electrochemical techniques like cyclic voltammetry (CV), electrochemical impedance spectroscopy (EIS), chronoamperometry (CA) studies were performed to evaluate the efficiency of prepared metal oxide thin films for methanol oxidation. NiO-$Y_2O_3$/FTO thin film showed current density value of 7 $mA/cm^2$ vs. 0.65V in cathodic half cycle with 0.8 M methanol solution at scan rate of 100mV/s. NiO-$ZrO_2$/FTO thin film showed current density value of 10 $mA/cm^2$ vs. 0.65 V with 0.6 M methanol solution at scan rate of 100mV/s. Comparatively, pure NiO, $Y_2O_3$ and $ZrO_2$ observed no prominent oxidation peaks which is attributed to the synergistic effect between metal oxides in mixed metal oxide thin films.

Furthermore, it was found that with increase in methanol concentration and scan rate current densities of the prepared thin films increases, which inferred that oxidation of methanol is diffusion-controlled process and increase in scan rate increases electron transfer process which ultimately enhances the peak current density. Concentration studies revealed that thin films with 0.1: 0.1 (NiO: $Y_2O_3/ZrO_2$) precursor concentration showed best results with oxidation peak at the lowest oxidation potential and lowest onset potential. Current-time plot

was obtained to check the stability of prepared thin films towards methanol oxidation. NiO-$ZrO_2$/FTO and NiO-$Y_2O_3$/FTO thin films observed current decay of 10% and 6.8% of initial current density values. This decay may be due to the reduction of methanol concentration near electrode surface with time or due to accumulation of carbonaceous reaction intermediates like CO on electrode surface. Electrochemical impedance studies were conducted to further evaluate the electrocatalytic performance of prepared films. Nyquist plot of NiO-$ZrO_2$/FTO showed decreased $R_{ct}$ value of 34.14Ω compared to pure NiO and $ZrO_2$ with $R_{ct}$ values of 88.42Ω and 2779Ω respectively. Nyquist plot of NiO-$Y_2O_3$/FTO showed decreased $R_{ct}$ value of 22.8Ω compared to pure NiO and $Y_2O_3$ with $R_{ct}$ values of 88.4Ω and 3189Ω respectively. These mixed metal oxide thin films showed enhanced catalytic performance, high stability and reusability which make them the best alternatives for methanol oxidation reactions.

## References


1. Pudukudy, M.; Yaakob, Z.; Mohammad, M.; Narayanan, B.; Sopian, K., Renewable hydrogen economy in Asia–Opportunities and challenges: An overview. *Renewable and Sustainable Energy Reviews* **2014,** *30*, 743-757.
2. Wolfram, C.; Shelef, O.; Gertler, P., How will energy demand develop in the developing world? *Journal of Economic Perspectives* **2012,** *26* (1), 119-38.
3. OECD, I., Energy and Air Pollution: World Energy Outlook Special Report 2016. **2016**.
4. Stocker, T. F., D. Qin, G.-K. Plattner, M. Tignor, S.K. Allen, J. Boschung, A. Nauels, Y. Xia, V. Bex and P.M. Midgley (eds.) Climate Change 2013: The Physical Science Basis. Contribution of Working Group I to the Fifth Assessment Report of the Intergovernmental Panel on Climate Change. https://www.ipcc.ch/report/ar5/wg1/.
5. Hu, J.; Galvita, V. V.; Poelman, H.; Marin, G. B., Advanced Chemical Looping Materials for CO(2) Utilization: A Review. *Materials* **2018,** *11* (7). PAGE number?
6. Kirubakaran, A.; Jain, S.; Nema, R. K., A review on fuel cell technologies and power electronic interface. *Renewable and Sustainable Energy Reviews* **2009,** *13* (9), 2430-2440.
7. Escudero-Escribano, M. Electrocatalysis and surface nanostructuring : atomic ensemble effects and non-covalent interactions. 2011.
8. (a) Kamarudin, S. K.; Daud, W. R. W.; Ho, S. L.; Hasran, U. A., Overview on the challenges and developments of micro-direct methanol fuel cells (DMFC). *J. Power Sources* **2007,** *163* (2), 743-754; (b) Verma, L., Studies on methanol fuel cell. *J. Power Sources* **2000,** *86* (1-2), 464-468.
9. Yuda, A.; Ashok, A.; Kumar, A., A comprehensive and critical review on recent progress in anode catalyst for methanol oxidation reaction. *Catalysis Reviews* **2020**, 1-103.
10. Yu, E. H.; Krewer, U.; Scott, K., Principles and materials aspects of direct alkaline alcohol fuel cells. *Energies* **2010,** *3* (8), 1499-1528.
11. Mahapatra, S.; Datta, J., Characterization of Pt-Pd/C electrocatalyst for methanol oxidation in alkaline medium. *International Journal of Electrochemistry* **2011,** *2011*.
12. Matsuoka, K.; Iriyama, Y.; Abe, T.; Matsuoka, M.; Ogumi, Z., Electro-oxidation of methanol and ethylene glycol on platinum in alkaline solution: Poisoning effects and product analysis. *Electrochim. Acta* **2005,** *51* (6), 1085-1090.
13. Manoharan, R.; Prabhuram, J., Possibilities of prevention of formation of poisoning species on direct methanol fuel cell anodes. *J. Power Sources* **2001,** *96* (1), 220-225.
14. Tiwari, J. N.; Tiwari, R. N.; Singh, G.; Kim, K. S., Recent progress in the development of anode and cathode catalysts for direct methanol fuel cells. *Nano Energy* **2013,** *2* (5), 553-578.
15. Tang, Y.; Cheng, W., Nanoparticle-modified electrode with size-and shape-dependent electrocatalytic activities. *Langmuir* **2013,** *29* (9), 3125-3132.
16. (a) Hosseini, M. G.; Abdolmaleki, M.; Ashrafpoor, S., Methanol electro-oxidation on a porous nanostructured Ni/Pd-Ni electrode in alkaline media. *Chinese Journal of Catalysis* **2013,** *34* (9), 1712-1719; (b) Ogumi, Z.; Matsuoka, K.; Chiba, S.; Matsuoka, M.; Iriyama, Y.; Abe, T.; Inaba, M., Preliminary Study on Direct Alcohol Fuel Cells Employing Anion Exchange Membrane. *Electrochemistry* **2002,** *70* (12), 980-983; (c) Serov, A.; Kwak, C., Review of non-platinum anode catalysts for DMFC and PEMFC application. *Applied Catalysis B: Environmental* **2009,** *90* (3), 313-320.
17. Wang, Y.; Li, L.; Hu, L.; Zhuang, L.; Lu, J.; Xu, B., A feasibility analysis for alkaline membrane direct methanol fuel cell: thermodynamic disadvantages versus kinetic advantages. *Electrochem. Commun.* **2003,** *5* (8), 662-666.
18. Kim, S.; Park, S.-J., Electroactivity of Pt–Ru/polyaniline composite catalyst-electrodes prepared by electrochemical deposition methods. *Solid State Ionics* **2008,** *178* (37), 1915-1921.

19. Li, Y.; Liu, C.; Liu, Y.; Feng, B.; Li, L.; Pan, H.; Kellogg, W.; Higgins, D.; Wu, G., Sn-doped TiO2 modified carbon to support Pt anode catalysts for direct methanol fuel cells. *J. Power Sources* **2015,** *286*, 354-361.
20. Mu, X.; Xu, Z.; Xie, Y.; Mi, H.; Ma, J., Pt nanoparticles supported on Co embedded coal-based carbon nanofiber for enhanced electrocatalytic activity towards methanol electro-oxidation. *J. Alloys Compd.* **2017,** *711*, 374-380.
21. Long, G.-f.; Li, X.-h.; Wan, K.; Liang, Z.-x.; Piao, J.-h.; Tsiakaras, P., Pt/CN-doped electrocatalysts: Superior electrocatalytic activity for methanol oxidation reaction and mechanistic insight into interfacial enhancement. *Applied Catalysis B: Environmental* **2017,** *203*, 541-548.
22. (a) Zhang, J.-M.; Sun, S.-N.; Li, Y.; Zhang, X.-J.; Zhang, P.-Y.; Fan, Y.-J., A strategy in deep eutectic solvents for carbon nanotube-supported PtCo nanocatalysts with enhanced performance toward methanol electrooxidation. *Int. J. Hydrogen Energy* **2017,** *42* (43), 26744-26751; (b) Ning, L.; Liu, X.; Deng, M.; Huang, Z.; Zhu, A.; Zhang, Q.; Liu, Q., Palladium-based nanocatalysts anchored on CNT with high activity and durability for ethanol electro-oxidation. *Electrochim. Acta* **2019,** *297*, 206-214; (c) Zhao, L.; Sui, X.-L.; Li, J.-Z.; Zhang, J.-J.; Zhang, L.-M.; Huang, G.-S.; Wang, Z.-B., Supramolecular assembly promoted synthesis of three-dimensional nitrogen doped graphene frameworks as efficient electrocatalyst for oxygen reduction reaction and methanol electrooxidation. *Applied Catalysis B: Environmental* **2018,** *231*, 224-233.
23. Tang, J.; Liu, J.; Torad, N. L.; Kimura, T.; Yamauchi, Y., Tailored design of functional nanoporous carbon materials toward fuel cell applications. *Nano Today* **2014,** *9* (3), 305-323.
24. Jeon, Y.; Ji, Y.; Cho, Y. I.; Lee, C.; Park, D.-H.; Shul, Y.-G., Oxide–carbon nanofibrous composite support for a highly active and stable polymer electrolyte membrane fuel-cell catalyst. *ACS nano* **2018,** *12* (7), 6819-6829.
25. Ji, Y.; Cho, Y. i.; Jeon, Y.; Lee, C.; Park, D.-H.; Shul, Y.-G., Design of active Pt on TiO2 based nanofibrous cathode for superior PEMFC performance and durability at high temperature. *Applied Catalysis B: Environmental* **2017,** *204*, 421-429.
26. Chhina, H. Oxidation resistant catalyst support for proton exchange membrane fuel cells. 2009.
27. Kim, J. M.; Lee, Y. J.; Kim, S.-h.; Chae, K.-H.; Yoon, K. R.; Lee, K. A.; Byeon, A.; Kang, Y. S.; Park, H.-Y.; Cho, M. K.; Ham, H. C.; Kim, J. Y., High-performance corrosion-resistant fluorine-doped tin oxide as an alternative to carbon support in electrodes for PEM fuel cells. *Nano Energy* **2019,** *65*, 104008.
28. Rigo, V. A.; Miranda, C. R.; Baletto, F., Ethanol chemisorption on core–shell Pt-nanoparticles: an ab initio study. *The European Physical Journal B* **2019,** *92* (2), 24.
29. Zhang, Y.; Bu, L.; Jiang, K.; Guo, S.; Huang, X., Concave Pd-Pt Core-Shell Nanocrystals with Ultrathin Pt Shell Feature and Enhanced Catalytic Performance. *Small (Weinheim an der Bergstrasse, Germany)* **2016,** *12* (6), 706-12.
30. Yang, Z.; Pedireddy, S.; Lee, H. K.; Liu, Y.; Tjiu, W. W.; Phang, I. Y.; Ling, X. Y., Manipulating the d-Band Electronic Structure of Platinum-Functionalized Nanoporous Gold Bowls: Synergistic Intermetallic Interactions Enhance Catalysis. *Chem. Mater.* **2016,** *28* (14), 5080-5086.
31. Liu, H.-l.; Nosheen, F.; Wang, X., Noble metal alloy complex nanostructures: controllable synthesis and their electrochemical property. *Chem. Soc. Rev.* **2015,** *44* (10), 3056-3078.
32. Du, X.; Luo, S.; Du, H.; Tang, M.; Huang, X.; Shen, P. K., Monodisperse and self-assembled Pt-Cu nanoparticles as an efficient electrocatalyst for the methanol oxidation reaction. *Journal of Materials Chemistry A* **2016,** *4* (5), 1579-1585.
33. Wang, C.; Zhang, L.; Yang, H.; Pan, J.; Liu, J.; Dotse, C.; Luan, Y.; Gao, R.; Lin, C.; Zhang, J.; Kilcrease, J. P.; Wen, X.; Zou, S.; Fang, J., High-Indexed Pt3Ni Alloy Tetrahexahedral Nanoframes Evolved through Preferential CO Etching. *Nano Lett.* **2017,** *17* (4), 2204-2210.
34. Das, A.; Layek, R.; Kim, N. H.; Jung, D.; Lee, J., Reduced graphene oxide (RGO)-supported NiCo2O4 nanoparticles: An electrocatalyst for methanol oxidation. *Nanoscale* **2014,** *6*.

35. Wu, D.; Zhang, W.; Cheng, D., Facile Synthesis of Cu/NiCu Electrocatalysts Integrating Alloy, Core–Shell, and One-Dimensional Structures for Efficient Methanol Oxidation Reaction. *ACS applied materials & interfaces* **2017,** *9* (23), 19843-19851.
36. Yu, Y.; Yang, Q.; Li, X.; Guo, M.; Hu, J., A bimetallic Ni–Ti nanoparticle modified indium tin oxide electrode fabricated by the ion implantation method for studying the direct electrocatalytic oxidation of methanol. *Green Chemistry* **2016,** *18* (9), 2827-2833.
37. Luo, Q.; Peng, M.; Sun, X.; Asiri, A. M., Hierarchical nickel oxide nanosheet@nanowire arrays on nickel foam: an efficient 3D electrode for methanol electro-oxidation. *Catalysis Science & Technology* **2016,** *6* (4), 1157-1161.
38. Thamer, B. M.; El-Newehy, M. H.; Al-Deyab, S. S.; Abdelkareem, M. A.; Kim, H. Y.; Barakat, N. A. M., Cobalt-incorporated, nitrogen-doped carbon nanofibers as effective non-precious catalyst for methanol electrooxidation in alkaline medium. *Applied Catalysis A: General* **2015,** *498*, 230-240.
39. Yu, M.; Wang, S.; Hu, J.; Chen, Z.; Bai, Y.; Wu, L.; Chen, J.; Weng, X., Additive-free macroscopic-scale synthesis of coral-like nickel cobalt oxides with hierarchical pores and their electrocatalytic properties for methanol oxidation. *Electrochim. Acta* **2014,** *145*, 300-306.
40. Hori, Y.; Murata, A.; Yoshinami, Y., Adsorption of CO, intermediately formed in electrochemical reduction of $CO_2$, at a copper electrode. *J. Chem. Soc., Faraday Trans.* **1991,** *87* (1), 125-128.
41. Döner, A.; Solmaz, R.; Kardaş, G., Fabrication and characterization of alkaline leached CuZn/Cu electrode as anode material for direct methanol fuel cell. *Energy* **2015,** *90*, 1144-1151.
42. Martinu, L.; Zabeida, O.; Klemberg-Sapieha, J.; Martin, P., Handbook of deposition technologies for films and coatings. *Peter M. Martin. Published by Elsevier Inc* **2010**.
43. Martin, P. M., *Handbook of deposition technologies for films and coatings: science, applications and technology*. William Andrew: 2009.
44. Martin, P., *Introduction to surface engineering and functionally engineered materials*. John Wiley & Sons: 2011; Vol. 74.
45. Wasa, K.; Kitabatake, M.; Adachi, H., *Thin film materials technology: sputtering of control compound materials*. Springer Science & Business Media: 2004.
46. Livage, J.; Sanchez, C.; Henry, M.; Doeuff, S., The chemistry of the sol-gel process. *Solid State Ionics* **1989,** *32*, 633-638.
47. Tjong, S.; Chen, H., Nanocrystalline materials and coatings. *Materials Science and Engineering: R: Reports* **2004,** *45* (1-2), 1-88.
48. Scriven, L., Physics and applications of dip coating and spin coating. *MRS Online Proceedings Library Archive* **1988,** *121*.
49. Elgrishi, N.; Rountree, K. J.; McCarthy, B. D.; Rountree, E. S.; Eisenhart, T. T.; Dempsey, J. L., A practical beginner's guide to cyclic voltammetry. *J. Chem. Educ.* **2018,** *95* (2), 197-206.
50. Nnamchi, P. S.; Obayi, C. S., Electrochemical Characterization of Nanomaterials. In *Characterization of Nanomaterials*, Elsevier: 2018; pp 103-127.
51. McCarthy, B. D.; Martin, D. J.; Rountree, E. S.; Ullman, A. C.; Dempsey, J. L., Electrochemical Reduction of Brønsted Acids by Glassy Carbon in Acetonitrile—Implications for Electrocatalytic Hydrogen Evolution. *Inorg. Chem.* **2014,** *53* (16), 8350-8361.
52. Zhang, J.; Wu, J.; Zhang, H., *PEM fuel cell testing and diagnosis*. Newnes: 2013.
53. Mareci, D.; Bolat, G.; Izquierdo, J.; Crimu, C.; Munteanu, C.; Antoniac, I.; Souto, R. M., Electrochemical characteristics of bioresorbable binary MgCa alloys in Ringer's solution: Revealing the impact of local pH distributions during in-vitro dissolution. *Materials Science and Engineering: C* **2016,** *60*, 402-410.
54. Li, H.; Li, H.; Wu, S.; Liao, C.; Zhou, Z.; Liu, X.; Djurišić, A. B.; Xie, M.; Tang, C.; Shih, K., Facile synthesis, characterization, and electrochemical performance of multi-scale AgVO3 particles. *J. Alloys Compd.* **2016,** *674*, 56-62.
55. Thomas, S.; Thomas, R.; Zachariah, A. K.; Kumar, R., *Spectroscopic Methods for Nanomaterials Characterization*. Elsevier: 2017; Vol. 2.

56. Salame, P. H.; Pawade, V. B.; Bhanvase, B. A., Chapter 3 - Characterization Tools and Techniques for Nanomaterials. In *Nanomaterials for Green Energy*, Bhanvase, B. A.; Pawade, V. B.; Dhoble, S. J.; Sonawane, S. H.; Ashokkumar, M., Eds. Elsevier: 2018; pp 83-111.
57. Shanks, R. A., Chapter 2 - Characterization of Nanostructured Materials. In *Nanostructured Polymer Blends*, Thomas, S.; Shanks, R.; Chandrasekharakurup, S., Eds. William Andrew Publishing: Oxford, 2014; pp 15-31.
58. Xu, C.; Faghri, A.; Li, X.; Ward, T., Methanol and water crossover in a passive liquid-feed direct methanol fuel cell. *Int. J. Hydrogen Energy* **2010,** *35* (4), 1769-1777.
59. Chetty, R.; Scott, K.; Kundu, S.; Muhler, M., Optimization of mesh-based anodes for direct methanol fuel cells. *Journal of Fuel Cell Science and Technology* **2010,** *7* (3).
60. Bahrami, H.; Faghri, A., Exergy analysis of a passive direct methanol fuel cell. *J. Power Sources* **2011,** *196* (3), 1191-1204.
61. Shrivastava, N. K.; Thombre, S. B.; Chadge, R. B., Liquid feed passive direct methanol fuel cell: challenges and recent advances. *Ionics* **2016,** *22* (1), 1-23.
62. Mansoor, M. A.; Lim, S. P.; Yusof, F. B.; Ming, H. N., Propitious Escalation in Photocurrent Response from MnZnO3 Thin Films Using Methanol as Sacrificial Agent. *J. Electron. Mater.* **2019,** *48* (7), 4375-4380.
63. Munawar, K.; Mansoor, M.; Basirun, W.; Misran, M.; Huang, N. M.; Mazhar, M., Single step fabrication of Cuo Mno 2TiO2 composite thin films with improved photoelectrochemical response. *RSC Advances* **2017,** *7*, 15885-15893.
64. Munawar, K.; Mansoor, M. A.; Basirun, W. J.; Misran, M.; Huang, N. M.; Mazhar, M., Single step fabrication of CuO–MnO–2$TiO_2$ composite thin films with improved photoelectrochemical response. *RSC Advances* **2017,** *7* (26), 15885-15893.
65. Mansoor, M. A.; Mazhar, M.; Pandikumar, A.; Khaledi, H.; Nay Ming, H.; Arifin, Z., Photoelectrocatalytic activity of $Mn_2O_3$–$TiO_2$ composite thin films engendered from a trinuclear molecular complex. *Int. J. Hydrogen Energy* **2016,** *41* (22), 9267-9275.
66. Saroni, A.; Alizadeh, M.; Rahman, S. A.; Meevasana, W.; Goh, B. T., In-situ synthesis of $In_2O_3$-based heterojunction thin films for enhanced visible light photoelectrochemical performance. *J. Power Sources* **2020,** *480*, 228829.
67. Munawar, K.; Mansoor, M. A.; McKee, V.; Zaharinie, T.; Mohd Zubir, M. N.; Aspanut, Z.; Yusof, F. B.; Mazhar, M., Optical and photocatalytic properties of biomimetic cauliflowered Ca2Mn3O8–CaO composite thin films. *J. Solid State Chem.* **2020,** *290*, 121552.
68. Ahmed, S.; Mansoor, M. A.; Basirun, W. J.; Sookhakian, M.; Huang, N. M.; Mun, L. K.; Söhnel, T.; Arifin, Z.; Mazhar, M., The synthesis and characterization of a hexanuclear copper–yttrium complex for deposition of semiconducting CuYO2–0.5Cu2O composite thin films. *New J. Chem.* **2015,** *39* (2), 1031-1037.
69. Ehsan, M. A.; Hakeem, A. S.; Khaledi, H.; Mazhar, M.; Shahid, M. M.; Pandikumar, A.; Huang, N. M., Fabrication of CuO–1.5$ZrO_2$ composite thin film, from heteronuclear molecular complex and its electrocatalytic activity towards methanol oxidation. *RSC Advances* **2015,** *5* (126), 103852-103862.
70. Che Mat, A. N.; Sairi, N. A.; Basirun, W. J.; Rezayi, M.; Mat Teridi, M. A.; Mazhar, M., Photoelectrocatalytic oxidation of methanol over $RuO_2MnO_2Co_3O_4$ supported porous anatase under visible light irradiation. *Mater. Chem. Phys.* **2019,** *224*, 196-205.
71. Shahid, M. M.; Pandikumar, A.; Golsheikh, A. M.; Huang, N. M.; Lim, H. N., Enhanced electrocatalytic performance of cobalt oxide nanocubes incorporating reduced graphene oxide as a modified platinum electrode for methanol oxidation. *RSC Advances* **2014,** *4* (107), 62793-62801.
72. Lim, S. P.; Pandikumar, A.; Huang, N. M.; Lim, H. N., Silver/titania nanocomposite-modified photoelectrodes for photoelectrocatalytic methanol oxidation. *Int. J. Hydrogen Energy* **2014,** *39* (27), 14720-14729.

73. Chen, C.-S.; Pan, F.-M.; Yu, H.-J., Electrocatalytic activity of Pt nanoparticles on a karst-like Ni thin film toward methanol oxidation in alkaline solutions. *Applied Catalysis B: Environmental* **2011,** *104* (3), 382-389.
74. Özdokur, K. V.; Çırak, B. B.; Caglar, B.; Çırak, Ç.; Karadeniz, S. M.; Kılınç, T.; Erdoğan, Y.; Ekinci, A. E., Fabrication of TiO2/ZnO/Pt nanocomposite electrode with enhanced electrocatalytic activity for methanol oxidation. *Vacuum* **2018,** *155*, 242-248.
75. Jiang, X.; Gür, T. M.; Prinz, F. B.; Bent, S. F., Atomic Layer Deposition (ALD) Co-Deposited Pt−Ru Binary and Pt Skin Catalysts for Concentrated Methanol Oxidation. *Chem. Mater.* **2010,** *22* (10), 3024-3032.
76. Hoseini, S.; Bahrami, M.; Roushani, M., High CO tolerance of Pt/Fe/Fe2O3 nanohybrid thin film suitable for methanol oxidation in alkaline medium. *RSC Adv.* **2014,** *4*.
77. Ghalmi, Y.; Habelhames, F.; Sayah, A.; Bahloul, A.; Nessark, B.; Shalabi, M.; Nunzi, J. M., Capacitance performance of NiO thin films synthesized by direct and pulse potentiostatic methods. *Ionics* **2019,** *25* (12), 6025-6033.
78. Grier, D.; McCarthy, G., North Dakota state university. *Fargo, North Dakota, USA, ICDD grant-in-aid* **1991**.
79. Yang, H.; Li, C.; Tang, A. In *Synthesis and Characterization of Fluorine-Doped Tin Dioxide Nanocomposites*, Cham, Springer International Publishing: Cham, 2016; pp 1507-1514.
80. Danaee, I.; Jafarian, M.; Forouzandeh, F.; Gobal, F.; Mahjani, M., Electrocatalytic oxidation of methanol on Ni and NiCu alloy modified glassy carbon electrode. *Int. J. Hydrogen Energy* **2008,** *33* (16), 4367-4376.